# *Jumping-Droplet-Enhanced Condensation on Scalable Superhydrophobic Nanostructured Surfaces*

# Jumping-Droplet-Enhanced Condensation on Scalable Superhydrophobic Nanostructured Surfaces

Nenad Miljkovic,[1] Ryan Enright,[1,2,§] Youngsuk Nam,[1,3] Ken Lopez,[1] Nicholas Dou,[1] Jean Sack,[1] and Evelyn N. Wang[1,*]

[1]*Department of Mechanical Engineering, Massachusetts Institute of Technology, 77 Massachusetts Avenue, Cambridge, Massachusetts 02139, USA*
[2]*Stokes Institute, University of Limerick, Limerick, Ireland*
[3]*Kyung Hee University, Yongin, Korea*
[§]*Current address: Thermal Management and Eco-sustainability Research Group, Bell Labs Ireland, Alcatel-Lucent, Blanchardstown Business & Technology Park, Snugborough Rd, Dublin 15, Ireland*

*Address correspondence to enwang@mit.edu

**ABSTRACT:**

When droplets coalesce on a superhydrophobic nanostructured surface, the resulting droplet can jump from the surface due to the release of excess surface energy. If designed properly, these superhydrophobic nanostructured surfaces can not only allow for easy droplet removal at micrometric length scales during condensation but promise to enhance heat transfer performance. However, the rationale for the design of an ideal nanostructured surface, as well as heat transfer experiments demonstrating the advantage of this jumping behavior are lacking. Here, we show that silanized copper oxide surfaces created *via* a simple fabrication method can achieve highly efficient jumping-droplet condensation heat transfer. We experimentally demonstrated a 25% higher overall heat flux and 30% higher condensation heat transfer coefficient compared to state-of-the-art hydrophobic condensing surfaces at low supersaturations (<1.12). This work not only

shows significant condensation heat transfer enhancement, but promises a low cost and scalable approach to increase efficiency for applications such as atmospheric water harvesting and dehumidification. Furthermore, the results offer insights and an avenue to achieve high flux superhydrophobic condensation.

**KEYWORDS:**

Jumping droplets, nanostructure, superhydrophobic surface, enhanced condensation, condensation heat transfer

**LETTER:**

Condensation is a ubiquitous phase-change process that is an essential natural phenomenon and widely used in various industries. Enhancement of condensation heat and mass transfer promises considerable savings in energy and natural resources for applications including water harvesting,[1,2] desalination,[3] thermal management,[4] industrial power generation,[5] and building heating and cooling.[6,7] As a result, dropwise condensation with non-wetting substrates has attracted much attention since its discovery by Schmidt *et al.* in the early 1930s due to the potential for higher phase-change heat transfer performance when compared to filmwise condensation.[8,9] To achieve efficient dropwise condensation, however, condensate droplets must be rapidly removed from the surface because the increasing droplet size acts as a thermal barrier.[10] For traditional dropwise condensing surfaces, such removal typically relies on gravity, where droplet sizes have to approach the capillary length (≈2.7 mm for water) to overcome the contact line pinning force.[11,12]

A recent study on structured superhydrophobic surfaces, however, demonstrated that when small droplets (≈10-100 μm) merge on suitably designed superhydrophobic surfaces, they can undergo coalescence-induced droplet ejection or 'jumping' independent of gravity[13] due to the release of excess surface energy.[14] The nanostructured surface beneath the coalescing droplets reduces the droplet adhesion to the substrate by minimizing the solid fraction, and breaks the symmetry of the coalesced droplet.[13] As a result, the droplet accelerates and departs perpendicular to the surface. Such droplet jumping offers an avenue to further enhance condensation heat transfer over conventional dropwise condensation by increasing the time-averaged density of small droplets, which transfer heat more efficiently from the vapor to the substrate.[15-19] While a considerable amount of work has focused on understanding and fabricating structured surfaces to sustain droplet jumping,[13,15-18,20-27] heat transfer measurements that quantify the amount of enhancement possible using these surfaces are lacking. In addition, past studies have utilized surfaces that are relatively expensive to fabricate, typically require the use of a cleanroom environment, and generally are not applicable to arbitrarily shaped surfaces, which presents challenges in the eventual scale-up for large scale thermal applications.

In this work, we experimentally demonstrated that a 25% higher overall heat flux and 30% higher condensation heat transfer coefficient can be achieved using silanized copper oxide (CuO) superhydrophobic surfaces compared to conventional dropwise condensing copper (Cu) surfaces at low supersaturations ($S < 1.12$). We show that these CuO surfaces offer ideal condensation behavior in terms of emergent droplet morphology and coalescence dynamics, and a significant enhancement in heat transfer performance when compared to state-of-the-art condensing surfaces. Furthermore, the chemical-oxidation-based CuO fabrication process provides a simple and readily scalable method to create superhydrophobic condensation surfaces

that can sustain droplet jumping behavior. Accordingly, these surfaces are attractive for applications such as atmospheric water harvesting[1] and dehumidification[6] where the heat fluxes are relatively low and droplets can be maintained in a highly mobile state.

We investigated the heat transfer behavior of Cu tubes, which are representative of a typical heat exchanger geometry and material,[28,29] coated with functionalized CuO nanostructures. Figures 1a, b and c show top, side, and high resolution images of the CuO nanostructures, respectively. Chemical-oxidation-based CuO nanostructuring was chosen as the ideal fabrication method due to its self-limiting growth behavior and low characteristic oxide thickness ($h \approx 1$ μm, Figure 1b), promising a low parasitic conduction thermal resistance ($k_{CuO} \approx 20$ W/m·K).[30] In addition, the knife-like nanostructure features (≤10 nm, Figure 1c) ensure nucleation within the structure (as opposed to the tips of the structure) due to the increased energy barrier associated with nucleation on features similar in size to the critical nucleation radius ($r_c \leq 35$ nm for water and typical conditions). Therefore, the formation of partially wetting droplet morphologies, which are essential to minimizing individual droplet thermal resistance,[18,31] are favored since Gibb's criterion can be satisfied.[32,33] Furthermore, the small characteristic length scale of the nanostructure spacing (≈1μm, Figure 1a) allows for higher nucleation densities, thus higher supersaturations prior to surface flooding, typically seen on larger scale microstructured surfaces.[21] From an industrial perspective, this fabrication method has several additional advantages: i) it can be applied to arbitrarily shaped surfaces, ii) the nanostructures can be formed over large areas, iii) the nanostructures form at low temperatures and do not require any high temperature annealing or drying processes and iv) the oxide growth mechanism is self-limiting, creating a uniform and thin nanostructure layer

independent of oxidation time.[34] Once the CuO surface is chemically functionalized (Figure 1d, Table 1), coalescence induced droplet jumping is stable and frequent.

We used commercially available oxygen-free Cu tubes (99.9 % purity) with outer diameters, $D_{OD}$ = 6.35 mm, inner diameters, $D_{ID}$ = 3.56 mm, and lengths $L$ = 131 mm as the test samples for the experiments. Each Cu tube was cleaned in an ultrasonic bath with acetone for 10 minutes and rinsed with ethanol, isopropyl alcohol and de-ionized (DI) water. The tubes were then dipped into a 2.0 M hydrochloric acid solution for 10 minutes to remove the native oxide film on the surface, then triple-rinsed with DI water, and dried with clean nitrogen gas.

Nanostructured CuO films were formed by immersing the cleaned tubes into a hot (96 ± 3 °C) alkaline solution composed of $NaClO_2$, NaOH, $Na_3PO_4 \bullet 12H_2O$, and DI water (3.75 : 5 : 10 : 100 wt.%).[17,34-36] During the oxidation process, a thin (≈300 nm) $Cu_2O$ layer was formed that then re-oxidized to form sharp, knife-like CuO oxide structures with heights of $h \approx 1$ μm, solid fraction $\varphi \approx 0.023$ and roughness factor $r \approx 10$ (Figure 1a, b, and c, see supporting information, section S5). To verify the independence of oxide thickness on chemical oxidation time, four separate samples were made using oxidation times, $\tau$ = 5, 10, 20, and 45 minutes.

In addition to the nanostructured CuO tubes, we tested smooth Cu tubes silanized to be hydrophobic (dropwise) or plasma cleaned to be hydrophilic (filmwise) for benchmark comparisons. Smooth oxidized Cu surfaces were achieved by immersing the cleaned tubes into a room temperature solution of $H_2O_2$ (hydrogen peroxide, Sigma-Aldrich) for 20 minutes to form a thin (≈300 nm) $Cu_2O$ layer (see Supporting Information, section S5).

Hydrophobic functionalization of both the nanostructured CuO and smooth Cu tubes was obtained by depositing a fluorinated silane (trichloro(1H,1H,2H,2H-perfluorooctyl)silane,

Sigma-Aldrich) in the vapor phase. This self-assembled coating had a typical advancing angle of $\theta_a \approx 120^\circ$ when measured on a smooth reference surface (Table 1). While the silane deposition step thickens the nanostructures by ≈10 nm (due to polycondensation of chlorosilanes),[37] the general morphology was left unchanged (Figure 1d).

Individual droplet growth on the nanostructured CuO surfaces was characterized using environmental scanning electron microscopy (ESEM).[25,38-46] Figure 2 shows time-lapse images of condensation on the nanostructured CuO surface (see Supporting Information, videoS1). Droplets nucleated within the nanostructures and, while growing beyond the confines of the structures, their apparent contact angle increased as they developed a balloon-like shape with a liquid bridge at the base.[17] This pinning behavior is consistent with the calculated preferred wetting state $E^* = -1/(r \cdot \cos\theta_a) \approx 0.2 < 1$.[21] Furthermore, this formation of partially wetting droplets is crucial for maximizing individual droplet growth rates by minimizing the droplet-base thermal resistance.[22] Once droplets grew to diameters large enough to coalesce with neighboring droplets ($R \approx 7$ μm), frequent out of plane jumping droplets were observed.[13] In addition to the removal of coalescing droplets, smaller droplets located near the coalescing pair were also removed (Figure 2). This sweeping behavior created by coalescing droplet pairs is attributed to the inertially-driven shape change generated during coalescence which can stretch the droplet and result in coalescence with multiple neighboring droplets.[13,47]

To determine the overall condensation heat transfer performance, the CuO nanostructured tubes were tested in a controlled condensation chamber (Supporting Information, section S2). Prior to performing the experiments, the vapor supply of water was vigorously boiled and the test chamber was evacuated to a pressure $P < 0.5 \pm 0.025$ Pa to eliminate non-condensable gases.[9,48] Throughout the experiments, the chamber pressure and temperature were continuously

monitored to ensure saturated conditions. The temperature of the tube was independently controlled *via* a cooling loop, and inlet and outlet tube temperatures were measured to determine the condensation heat flux (Figure 3a). The vapor pressure range tested (2 kPa < $P_v$ < 3.6 kPa) corresponds to steam saturation temperatures of 17.5˚C - 27˚C, which are very common conditions for building energy, dehumidification and high efficiency industrial condenser applications.[49,50] Typical inlet to outlet tube temperature differences ranged from 0.5 to 2.5˚C depending on the tube sample and vapor pressure.

Figure 3b shows an image obtained during filmwise condensation on the clean, smooth hydrophilic Cu tube. As expected, vapor condensed and formed a thin liquid film that covered the entire surface (see Supporting Information, videoS2).[51] Meanwhile, Figure 3c shows an image during conventional dropwise condensation on the smooth hydrophobic Cu tube where discrete droplets formed and grew to sizes approaching the capillary length (≈2.7 mm) before being removed by gravity (see Supporting Information, videoS3).[51] The condensation mechanism on both of the smooth Cu tubes (hydrophilic and hydrophobic) was independent of the supersaturation $S$, defined as the ratio of the vapor pressure to the saturation pressure corresponding to the sample surface temperature ($S = P_v/P_w$). In contrast, condensation on the nanostructured CuO surface showed significant dependence on the supersaturation. Figures 3d and e show images during condensation on the nanostructured CuO surface for low ($S$ = 1.08) and high ($S$ = 1.54) supersaturations, respectively (see Supporting Information, videoS4 and S5). At the low supersaturation (Figure 3d), the CuO surface showed very efficient droplet removal *via* the jumping mechanism, with numerous microscale droplets ($R \approx 8$ μm) populating the surface (see Supporting Information, section S5). However, as the supersaturation was increased to 1.54 (by lowering the cooling water temperature), the emergent droplet morphology

transitioned from highly mobile jumping droplets to highly pinned Wenzel droplets, which completely wet the cavities of the nanostructure. Figures 4a and b show time-lapse images of the jumping and flooding condensation mechanisms, respectively, during initial transient condensate formation. Note that the transition from jumping to Wenzel droplets on the surface was not reversible, *i.e.*, once flooding initiated, reduction of the supersaturation did not revert the behavior to droplet jumping. The only means to recover the droplet jumping mode was to increase the cooling water temperature enough to re-evaporate all of the condensate. This observed hysteresis in the heat transfer behavior indicates that the procedure used to obtain steady operation of the condensing surface is extremely important.

The hysteresis can be explained in terms of the interplay between the characteristic structure length scale and droplet nucleation density.[14,21] At low supersaturations ($S < 1.12$, low nucleation density), droplets formed with large spacings between each other relative to the spacing of the nanostructures such that the droplet could evolve into the energetically favorable partially wetting (PW) Cassie-like morphology (Figure 2).[17] For higher supersaturations ($S > 1.12$), the droplet nucleation density increased to the point where droplet/droplet interactions occurred on a similar length scale as the nanostructure spacing (≈1 μm), and droplets, instead of forming in the energetically favorable PW morphology, merged to form pinned liquid films due to contact line de-pinning at their base. Further condensation on the 'flooded' surface resulted in the formation of Wenzel droplets which demonstrated significant contact line pinning as evidenced by the large droplet shedding diameters. It is important to note that the critical radius for droplet nucleation at supersaturation conditions ($1.02 < S < 1.2$) which include jumping ($S < 1.12$) and flooding ($S > 1.12$) was 8 nm ($S = 1.2$) < $r_c$ < 41 nm ($S = 1.02$), which is much smaller than the characteristic structure length scale ($l \approx 1$ μm). The length scale discrepancy

($r_c << l$) implies that the flooding transition did not occur due to further reduction in $r_c$ as the supersaturation was increased ($S > 1.12$), since the critical nuclei were already well below the structure length scale.

Figure 5a shows the measured heat flux with the log mean water-to-vapor temperature difference ($\Delta T_{LMTD} = [(T_v - T_{in}) - (T_v - T_{out})]/ln[(T_v - T_{in})/(T_v - T_{out})]$, where $T_v$, $T_{in}$, and $T_{out}$ are the vapor, cooling water inlet and cooling water outlet temperatures, respectively) as a function of the condensation heat flux ($q$") at a vapor pressure $P_v = 2700 \pm 68$ Pa. To maximize the tube internal heat transfer coefficient, the cooling water mass flow rate was held constant at $5 \pm 0.1$ L/min for all experiments ($1.02 < S \leq 1.6$, $10 < T_s < 25$˚C, where $T_s$ is the extrapolated tube surface temperature, see Supporting Information, section S6). Condensation on the filmwise (diamond symbols) and dropwise (square symbols) Cu surfaces served as baseline cases for comparing condensation performance. The overall heat transfer coefficient (HTC), $\bar{U} = q"/\Delta T_{LMTD}$, was obtained from the slope. As expected, the Cu tube with filmwise behavior showed the worst overall HTC ($\bar{U}_{filmwise} = 8.92 \pm 1.14$ kW/m$^2$K) due to the thin liquid film acting as the dominant thermal resistance to heat transfer.[51] Meanwhile, the Cu tube with dropwise behavior showed improved performance over the filmwise tube ($\bar{U}_{dropwise} = 13.15 \pm 0.73$ kW/m$^2$K) because as discrete droplets roll off the surface by gravity they also sweep other droplets to clean the surface for re-nucleation.[9] The nanostructured CuO surface heat flux was highly dependent on the condensation mode (jumping or flooded), as discussed previously. When the jumping droplet removal mechanism was favored (star symbols, $S < 1.12$, $\Delta T_{LMTD} < 5$ K), the CuO tube showed the highest heat transfer performance ($\bar{U}_{jumping} = 16.5 \pm 2.20$ kW/m$^2$K), representing a 25% larger overall heat flux than the dropwise condensing surface. However, when the supersaturation increased to the point of flooding (empty

and filled triangle symbols, $S > 1.12$), the heat transfer performance reduced below that of the dropwise Cu sample ($\bar{U}_{\text{flooded}} = 10.1 \pm 0.98$ kW/m$^2$K) due to droplet pinning, but remained above that of the filmwise sample. The significant performance hysteresis of the CuO surface allowed for heat transfer measurements to be obtained at low supersaturations ($S < 1.12$) for the flooded regime (empty triangle symbols) by first flooding the surface and then progressively increasing the cooling water temperature to reduce the supersaturation.

We also investigated the effect of vapor pressure (2 kPa < $P_v$ < 3.6 kPa) on the overall heat transfer performance to provide further insight into the condensation process on these surfaces, as well as to demonstrate the applicability of these surfaces for systems requiring different operating conditions. Figure 5b shows the steady state condensation HTC at the tube surface, $h_c$, as a function of the chamber vapor pressure, $P_v$. First, to ensure the accuracy of our experimental results, we compared our baseline measurements to literature values, and showed that our measured filmwise and dropwise HTCs are in good agreement to those of Young *et al.* ($h_{\text{filmwise}} = 19 \pm 1.1$ kW/m$^2$K)[52] and Marto *et al.* ($h_{\text{dropwise}} = 75 \pm 15$ kW/m$^2$K)[53]. Accordingly, with the jumping condensation, we demonstrated a 30% higher HTC in comparison to dropwise condensation on the smooth Cu tube ($h_{\text{jumping}} = 92 \pm 12$ kW/m$^2$K). Meanwhile, flooding of the surface at higher supersaturations led to a 40% degradation compared to dropwise condensation on the smooth Cu tube ($h_{\text{flooded}} = 44 \pm 6$ kW/m$^2$K).

To explain the experimental results and investigate the heat transfer dependence on surface structure and vapor pressure, we used our developed model that incorporates thermal resistance based droplet growth, emergent droplet wetting morphology, and droplet distribution theory (see Supporting Information, section S7).[17,54] The results from the model (lines) shown in Figure 5b are in excellent agreement with the experiments (symbols). For the jumping and

flooded performance, the model results were obtained using experimentally determined droplet departure radii $\hat{R}$ ($\hat{R}_{dropwise} \approx 1.3$ mm, $\hat{R}_{jumping} \approx 7$ μm, $\hat{R}_{flooded} \approx 2$ mm), contact angles, and a nucleation density $N$ estimated based on previous ESEM studies of condensation on these CuO surfaces ($N_{nanostructured} \approx 3N_{smooth}$).[17] The significant enhancement of the condensation heat transfer coefficient demonstrated with the jumping CuO surface, compared to the smooth dropwise and flooded CuO surfaces, is explained as follows. The increased number of smaller droplets maintains a smaller conduction resistance and ≈50% enhanced condensation heat transfer performance when compared to smooth dropwise condensing surfaces.[17,18] This result was obtained by incorporating the average steady state droplet size distribution for the jumping droplet surface, $2R = 7.6 \pm 2.2$ μm (see Figure 2 and Supporting Information, section S5), into our model. In addition, the formation of the PW droplet morphology during condensation decreases the composite thermal resistance beneath the droplet, and together with the jumping removal mechanism further enhances the heat transfer. However, after flooding, the heat transfer degrades because the increased pinning force at the contact line of the Wenzel droplets inhibits jumping and gravity is required to shed droplets from the surface. Accordingly, these droplets need to grow to sizes two orders of magnitude larger than in the jumping mode before being removed, leading to an increased population of large droplets which have a higher conduction thermal resistance and, consequently, reduce the heat transfer coefficient. The modeling results for the flooded sample show that the larger average droplet departure radius ($\hat{R}_{flooded} = 2$ mm) is primarily responsible for the ≈40% lower heat transfer performance when compared to the dropwise sample. However, there is also an additional effect associated with large pinned droplets at the bottom of the tube sample that effectively insulates up to 15% of the surface (Figure 3e), thus contributing to the performance discrepancy of the flooded sample compared to

the dropwise sample. Finally, the jumping surface showed stronger pressure dependence, in both the model and experiment, when compared to the other surface types. This result is due to the fact that during individual droplet growth at small sizes ($R < 7$ μm), the droplet conduction resistance is smaller than the interfacial mass transfer resistance. Accordingly, in the case of jumping surfaces, the majority of the condensing droplets sizes were small enough ($R < 7$ μm) such that the interfacial mass transfer resistance, which is sensitive to vapor pressure,[51] became comparable to the conduction resistance. Therefore, the heat transfer coefficient of the jumping surface varied more with vapor pressure than that of the other surfaces.

The outcomes of this work support the findings that both the droplet removal method (jumping versus gravitational shedding) and the emergent droplet morphology are critical in realizing enhanced condensation heat and mass transfer over state-of-the-art dropwise condensing surfaces. Furthermore, the experimental results suggest that nanostructured superhydrophobic surfaces have limitations for high heat flux applications due to progressive flooding of the surface and the formation of highly pinned liquid droplets. Although the presented results show the CuO nanostructure are ideal in terms of creating efficient droplet jumping and offer considerable heat transfer enhancement, the identified flooding mechanism presents a need for further reduction in the structure scale and/or reduction and control of the nucleation density at elevated supersaturations *via* engineering of the hydrophobic coating at length scales on the order of 10 nm or less. In addition, the CuO surfaces in this work present an opportunity to enhance condensation in the presence of non-condensable gasses (NCGs) due to the potential for significant boundary layer mixing created by high frequency droplet jumping. Much work has been done to show the importance of vapor flow and droplet shedding on condensation heat transfer enhancement in the presence of NCGs *via* boundary layer

mixing.[48,55,56] These surfaces therefore promise opportunities for applications such as water harvesting, desalination or dehumidification, where the relative driving potential for condensation is low and NCGs are present.[57]

In summary, we experimentally demonstrated that by using readily scalable nanostructured CuO surfaces, water condensation with droplet jumping can be achieved while minimizing the parasitic thermal resistances (oxide thickness). As a result, 25% higher overall heat flux and 30% higher condensation heat transfer coefficients compared to state-of-the-art dropwise condensing Cu surfaces were realized at low heat fluxes and correspondingly, low supersaturations ($S < 1.12$). At high supersaturations ($S > 1.12$), flooding of the nanostructured surfaces led to the formation of highly pinned Wenzel droplets, which degraded the condensation heat transfer coefficient by 40% compared to the smooth dropwise condensing tube. These results provide guidelines for the fabrication of high performance nanostructured CuO surfaces for low condensation heat flux applications. Furthermore, the results underscore the importance of the operating conditions for condensation heat and mass transfer on nanostructured superhydrophobic surfaces and also provide insights into the surface design requirements for high heat flux applications.

**References:**


1 Andrews, H. G., Eccles, E. A., Schofield, W. C. E. & Badyal, J. P. S. Three-Dimensional Hierarchical Structures for Fog Harvesting. *Langmuir* **27**, 3798-3802, (2011).

2 Milani, D., Abbas, A., Vassallo, A., Chiesa, M. & Al Bakri, D. Evaluation of Using Thermoelectric Coolers in a Dehumidification System to Generate Freshwater From Ambient Air. *Chem Eng Sci* **66**, 2491-2501, (2011).

3 Khawaji, A. D., Kutubkhanah, I. K. & Wie, J. M. Advances in seawater desalination technologies. *Desalination* **221**, 47-69, (2008).

4 Kim, M. H. & Bullard, C. W. Air-side performance of brazed aluminum heat exchangers under dehumidifying conditions. *Int J Refrig* **25**, 924-934, (2002).

5 Beer, J. M. High efficiency electric power generation: The environmental role. *Prog Energ Combust* **33**, 107-134, (2007).

6 Perez-Lombard, L., Ortiz, J. & Pout, C. A review on buildings energy consumption information. *Energ Buildings* **40**, 394-398, (2008).

7 Li, B. Z. & Yao, R. M. Urbanisation and its impact on building energy consumption and efficiency in China. *Renew Energ* **34**, 1994-1998, (2009).

8 Schmidt, E., Schurig, W. & Sellschopp, W. Versuche über die Kondensation von Wasserdampf in Film- und Tropfenform. *Forsch. Ingenieurwes* **1**, 53–63, (1930).

9 Rose, J. W. Dropwise condensation theory and experiment: a review. *P I Mech Eng a-J Pow* **216**, 115-128, (2002).

10 Rose, J. W. On the Mechanism of Dropwise Condensation. *Int J Heat Mass Tran* **10**, 755-762, (1967).

11 Kim, H. Y., Lee, H. J. & Kang, B. H. Sliding of Liquid Drops Down an Inclined Solid Surface. *J Colloid Interf Sci* **247**, 372-380, (2002).

12 Dimitrakopoulos, P. & Higdon, J. J. L. On The Gravitational Displacement of Three-Dimensional Fluid Droplets From Inclined Solid Surfaces. *J Fluid Mech* **395**, 181-209, (1999).

13 Boreyko, J. B. & Chen, C. H. Self-Propelled Dropwise Condensate on Superhydrophobic Surfaces. *Phys Rev Lett* **103**, 184501-184501 - 184501-184504, (2009).

14 Lafuma, A. & Quere, D. Superhydrophobic States. *Nature Materials* **2**, 457-460, (2003).

15 Chen, X. *et al.* Nanograssed Micropyramidal Architectures for Continuous Dropwise Condensation. *Adv Funct Mater* **21**, 4617–4623, (2011).

16 Dietz, C., Rykaczewski, K., Fedorov, A. G. & Joshi, Y. Visualization of Droplet Departure on a Superhydrophobic Surface and Implications to Heat Transfer Enhancement During Dropwise Condensation. *Appl Phys Lett* **97**, 033104-033101 - 033104-033103, (2010).

17 Enright, R., Dou, N., Miljkovic, N., Nam, Y. & Wang, E. N. Condensation on Superhydrophobic Copper Oxide Nanostructures. *3rd Micro/Nanoscale Heat & Mass Transfer International Conference*, (2012).

18 Miljkovic, N., Enright, R. & Wang, E. N. Effect of Droplet Morphology on Growth Dynamics and Heat Transfer during Condensation on Superhydrophobic Nanostructured Surfaces. *Acs Nano* **6**, 1776–1785, (2012).

19 Rykaczewski, K. *et al.* Three Dimensional Aspects of Droplet Coalescence During Dropwise Condensation on Superhydrophobic Surfaces. *Soft Matter* **7**, 8749-8752, (2011).

20 Boreyko, J. B., Zhao, Y. J. & Chen, C. H. Planar jumping-drop thermal diodes. *Appl Phys Lett* **99**, (2011).
21 Enright, R., Miljkovic, N., Al-Obeidi, A., Thompson, C. V. & Wang, E. N. Superhydrophobic Condensation: The Role of Length Scale and Energy Barriers. *Langmuir* **40**, 14424–14432, (2012).
22 Miljkovic, N., Enright, R. & Wang, E. N. Growth Dynamics During Dropwise Condensation on Nanostructured Superhydrophobic Surfaces. *3rd Micro/Nanoscale Heat & Mass Transfer International Conference*, (2012).
23 Narhe, R. D., Khandkar, M. D., Shelke, P. B., Limaye, A. V. & Beysens, D. A. Condensation-Induced Jumping Water Drops. *Phys Rev E* **80**, 031604-031601 - 031604-031605, (2009).
24 Rykaczewski, K. Microdroplet Growth Mechanism during Water Condensation on Superhydrophobic Surfaces. *Langmuir* **28**, 7720-7729, (2012).
25 Rykaczewski, K. & Scott, J. H. J. Methodology for Imaging Nano-to-Microscale Water Condensation Dynamics on Complex Nanostructures. *Acs Nano* **5**, 5962-5968, (2011).
26 Rykaczewski, K. *et al.* How nanorough is rough enough to make a surface superhydrophobic during water condensation? *Soft Matter* **8**, 8786-8794, (2012).
27 Liu, T. Q., Sun, W., Sun, X. Y. & Ai, H. R. Mechanism study of condensed drops jumping on super-hydrophobic surfaces. *Colloids and Surfaces A: Physicochemical and Engineering Aspects*, (2012).
28 Kim, S. & Kim, K. J. Dropwise Condensation Modeling Suitable for Superhydrophobic Surfaces. *J Heat Transf* **133**, 081502-081501 - 081502-081507, (2011).
29 Incropera, F. P. & DeWitt, D. P. *Fundamentals of heat and mass transfer*. 2nd edn, (Wiley, 1985).
30 Kwak, K. & Kim, C. Viscosity and thermal conductivity of copper oxide nanofluid dispersed in ethylene glycol. *Korea-Aust Rheol J* **17**, 35-40, (2005).
31 Cao, L. L., Jones, A. K., Sikka, V. K., Wu, J. Z. & Gao, D. Anti-Icing Superhydrophobic Coatings. *Langmuir* **25**, 12444-12448, (2009).
32 Gibbs, J. W., Bumstead, H. A. & Van Name, R. G. *The scientific papers of J. Willard Gibbs*. (New York and Bombay, Longmans, Green and co., 1906).
33 Quere, D. Wetting and roughness. *Annu Rev Mater Res* **38**, 71-99, (2008).
34 Nam, Y. & Sungtaek, Y. A comparative study of the morphology and wetting characteristics of micro/nanostructured Cu surfaces for phase change heat transfer applications. *Journal of Adhesion Science and Technology*, 1-14, (2012).
35 Nam, Y. & Ju, Y. S. Comparative Study of Copper Oxidation Schemes and Their Effects on Surface Wettability. *Imece 2008: Heat Transfer, Fluid Flows, and Thermal Systems, Vol 10, Pts a-C*, 1833-1838, (2009).
36 Nam, Y., Sharratt, S., Byon, C., Kim, S. J. & Ju, Y. S. Fabrication and Characterization of the Capillary Performance of Superhydrophilic Cu Micropost Arrays. *Journal of Microelectromechanical Systems* **19**, 581 - 588 (2010).
37 Fadeev, A. Y. & McCarthy, T. J. Self-Assembly Is Not the Only Reaction Possible between Alkyltrichlorosilanes and Surfaces: Monomolecular and Oligomeric Covalently Attached Layers of Dichloro- and Trichloroalkylsilanes on Silicon. *Langmuir* **16**, 7268-7274, (2000).

38 Dietz, C., Rykaczewski, K., Fedorov, A. & Joshi, Y. ESEM Imaging of Condensation on a Nanostructured Superhydrophobic Surface. *J Heat Trans-T Asme* **132**, 080904-080901, (2010).
39 Miljkovic, N., Enright, R., Maroo, S. C., Cho, H. J. & Wang, E. N. Liquid Evaporation on Superhydrophobic and Superhydrophilic Nanostructured Surfaces. *J Heat Transf* **133**, 080903-080901, (2011).
40 Rykaczewski, K., Scott, J. H. J. & Fedorov, A. G. Electron Beam Heating Effects During Environmental Scanning Electron Microscopy Imaging of Water Condensation on Superhydrophobic Surfaces. *Appl Phys Lett* **98**, 093106-093101 - 093106-093103, (2011).
41 Rykaczewski, K. *et al.* Dynamics of Nanoparticle Self-Assembly into Superhydrophobic Liquid Marbles During Water Condensation. *Acs Nano* **5**, 9746–9754, (2011).
42 Anand, S. & Son, S. Y. Sub-Micrometer Dropwise Condensation Under Superheated and Rarefied Vapor Condition. *Langmuir* **26**, 17100-17110, (2010).
43 Varanasi, K. K. & Deng, T. in *12th Ieee Intersociety Conference on Thermal and Thermomechanical Phenomena in Electronic Systems* 1-5 (Los Vegas, NV, 2010).
44 Varanasi, K. K., Hsu, M., Bhate, N., Yang, W. S. & Deng, T. Spatial Control in the Heterogeneous Nucleation of Water. *Appl Phys Lett* **95**, 094101-094101 - 094101-094103, (2009).
45 Anderson, D. M. *et al.* Using Amphiphilic Nanostructures To Enable Long-Range Ensemble Coalescence and Surface Rejuvenation in Dropwise Condensation. *Acs Nano* **6**, 3262-3268, (2012).
46 Cheng, J., Vandadi, A. & Chen, C. L. Condensation heat transfer on two-tier superhydrophobic surfaces. *Appl Phys Lett* **101**, 131909-131901 - 131909-131904, (2012).
47 Blanchette, F. & Bigioni, T. P. Partial coalescence of drops at liquid interfaces. *Nat Phys* **2**, 254-257, (2006).
48 Ma, X. H., Zhou, X. D., Lan, Z., Li, Y. M. & Zhang, Y. Condensation Heat Transfer Enhancement in the Presence of Non-Condensable Gas Using the Interfacial Effect of Dropwise Condensation. *Int J Heat Mass Tran* **51**, 1728-1737, (2008).
49 Vosough, A. *et al.* Improvement Power Plant Efficiency with Condenser Pressure. *Iinternational Journal of Multidisciplinary Sciences and Engineering* **2**, 38-43, (2011).
50 Bejan, A. Fundamentals of exergy analysis, entropy generation minimization, and the generation of flow architecture. *Int J Energ Res* **26**, 545-565, (2002).
51 Carey, V. P. *Liquid-Vapor Phase-Change Phenomena: An Introduction to the Thermophysics of Vaporization and Condensation Processes in Heat Transfer Equipment*. 2nd edn, (Taylor and Francis, 2008).
52 Young, E. H. & Briggs, D. E. The Condensing of Low Pressure Steam on Vertical Rows of Horizontal Copper and Titanium Tubes. *A.I.Ch.E. Journal* **12**, 31-35, (1966).
53 Marto, P. J., Looney, D. J., Rose, J. W. & Wanniarachchi, A. S. Evaluation of Organic Coatings for the Promotion of Dropwise Condensation of Steam. *Int J Heat Mass Tran* **29**, 1109-1117, (1986).
54 Miljkovic, N., Enright, R. & Wang, E. N. Modeling and Optimization of Condensation Heat Transfer on Micro and Nanostructured Superhydrophobic Surfaces. *J Heat Transf*, (2012).

55 Rose, J. W. Approximate equation for forced convection in thepresence of non-condensable gas on flat plate and horizontal tube. *Int J Heat Mass Tran* **23**, 539-546, (1980).
56 Maheshwari, N. K., Saha, D., Sinha, R. K. & Ritomi, M. Investigation oncondensation in presence of a noncondensable gas for a wide range of Reynolds number. *Nuclear Engineering Design* **227**, 219-238, (2004).
57 Thiel, G. P. & Lienhard, J. H. Entropy generation in condensation in the presence of high concentrations of noncondensable gases. *Int J Heat Mass Tran* **55**, 5133-5147, (2012).

**Acknowledgements:** We gratefully acknowledge funding support from the MIT S3TEC Center, an Energy Frontier Research Center funded by the Department of Energy, Office of Science, Office of Basic Energy Sciences. We also acknowledge the support from the National Science Foundation through the Major Research Instrumentation Grant for Rapid Response Research (MRI-RAPID) for the microgoniometer. This work was performed in part at the Center for Nanoscale Systems (CNS), a member of the National Nanotechnology Infrastructure Network (NNIN), which is supported by the National Science Foundation under NSF award no. ECS-0335765. CNS is part of Harvard University. R.E. acknowledges funding received from the Irish Research Council for Science, Engineering, and Technology, cofunded by Marie Curie Actions under FP7.

**Supporting Information Available**: Five videos showing all condensation processes, as well as further information on data collection methodology, the experimental setup/procedure, and condensation modeling. This material is available free of charge via the Internet at http://pubs.acs.org.

**Author contributions**

N.M., R.E., Y.N. and E.N.W. conceived the initial idea of this research. E.N.W. guided the work. N.M., R.E., N.D., K.L., and J.S. carried out the experiments and collected data. N.M., R.E. and

E.N.W. were responsible for writing the paper. N.M. carried out the theoretical analysis. N.M., K.L. and N.D. analyzed the data.

**Competing financial interests:** The authors declare no competing financial interests.

**Figure and table legends**

**Figure 1 – Nanostructure characterization.** Field emission scanning electron microscopy (FESEM) images of a 5 minute CuO surface with (a) top view, no silane, (b) side view, no-silane (c) high magnification showing the blade structure of the oxide, no silane, and (d) high magnification after silane deposition. Due to imperfect monolayer formation, silane deposition thickens the oxide blades but maintains the general nanostructure morphology. The sharp, knife-like CuO structures have characteristic heights, $h \approx 1$ μm, solid fraction, $\varphi \approx 0.023$, and roughness factor, $r \approx 10$.

**Figure 2 – Droplet growth dynamics.** Time-lapse images captured *via* environmental scanning electron microscopy (ESEM) of steady state water condensation on a 10 minute CuO surface. A large viewing area was used to avoid electron beam heating effects. Condensing droplets underwent spontaneous droplet jumping and surface renewal. Light blue dotted circles highlight areas of the surface with droplets just prior to coalescence and subsequent jumping, while red dotted circles highlight areas of the surface right after droplet jumping ($P_v = 860 \pm 43$ Pa, $T_s = 4.5 \pm 1.5$ ˚C, $S = 1.02$, see Supporting Information, videoS1).

**Figure 3 – Test setup and experimental images of condensation.** (a) Schematic showing experimental setup. The tube sample ($D_{OD} = 6.35$ mm, $D_{ID} = 3.56$ mm, $L = 131$ mm) was cooled *via* chilled water flowing inside the tube at $5 \pm 0.1$ L/min. Images of (b) filmwise condensation on a smooth hydrophilic Cu tube, (c) dropwise condensation on a silane coated smooth Cu tube, (d) jumping-droplet superhydrophobic condensation on a nanostructured CuO tube (10 minute oxidation) (Inset: magnified view of the jumping phenomena, scale bar is 500 μm), and (d) flooded condensation on a nanostructured CuO tube. The tube dimensions are identical for each case (Chamber vapor pressure $P_v = 2700 \pm 68$ Pa).

**Figure 4 – Jumping and flooded condensation.** Time-lapse images of initial water condensation on a 10 minute oxidized CuO sample undergoing (a) jumping, ($S = 1.08$, $\Delta T_{LMTD} = 4$ K, $P_v = 2700 \pm 68$ Pa) and (b) flooded condensation ($S = 1.54$, $\Delta T_{LMTD} = 12$ K, $P_v = 2700 \pm 68$ Pa). Low supersaturations ($S = 1.08$) led to highly mobile partially wetting droplet formation and subsequent droplet jumping. High supersaturations ($S = 1.54$) led to surface flooding and the formation of highly pinned Wenzel droplet morphologies.

**Figure 5 – Heat transfer performance as a function of supersaturation and vapor pressure.** (a) Experimental steady state log mean water to vapor temperature difference ($\Delta T_{LMTD}$) as a function of overall surface heat flux ($q''$) for tube surfaces undergoing filmwise, dropwise, flooded, and jumping condensation (CuO chemical oxidation time $\tau = 10$ minutes, chamber vapor pressure $P_v = 2700 \pm 68$ Pa, $1.02 < S \leq 1.6$). Rapid droplet removal due to coalescence induced droplet jumping results in the highest heat fluxes for the jumping sample ($S < 1.12$). However, flooding of the surface at higher heat fluxes results in rapid performance degradation and transition into the flooded condensation mode ($S > 1.12$). Data for the flooded sample at low supersaturations ($S < 1.12$, open triangles) was obtained by flooding the surface and decreasing $\Delta T_{LMTD}$. Due to hysteresis, the jumping behavior was not recovered. (b) Experimental and theoretical steady state condensation coefficient ($h_c$) as a function of saturated vapor pressure ($P_v$) for tube surfaces undergoing filmwise, dropwise, flooded ($\tau = 5$, 10, 20 and 45 minutes), and

jumping ($\tau$ = 10 minutes) condensation (see Supporting Information, section S6). Jumping condensation shows the highest condensation HTC for low supersaturations ($S$ < 1.12). Error bars indicate the propagation of error associated with the fluid inlet and outlet temperatures (± 0.2 K) and pressure measurement (± 2.5 %). The jumping surface error bars are the largest due to the relatively low heat fluxes measured ($q$" < 80 kW/m$^2$), corresponding to the smaller fluid inlet to outlet temperature difference. The theoretical predictions (dotted lines) were obtained from the droplet growth and distribution model (For model derivation and parameters, see Supporting Information, Section S7).

**Table 1** – **Sample wetting characteristics.** Silane chemistry, tridecafluoro-1,1,2,2-tetrahydrooctyl)-1-trichlorosilane was used.

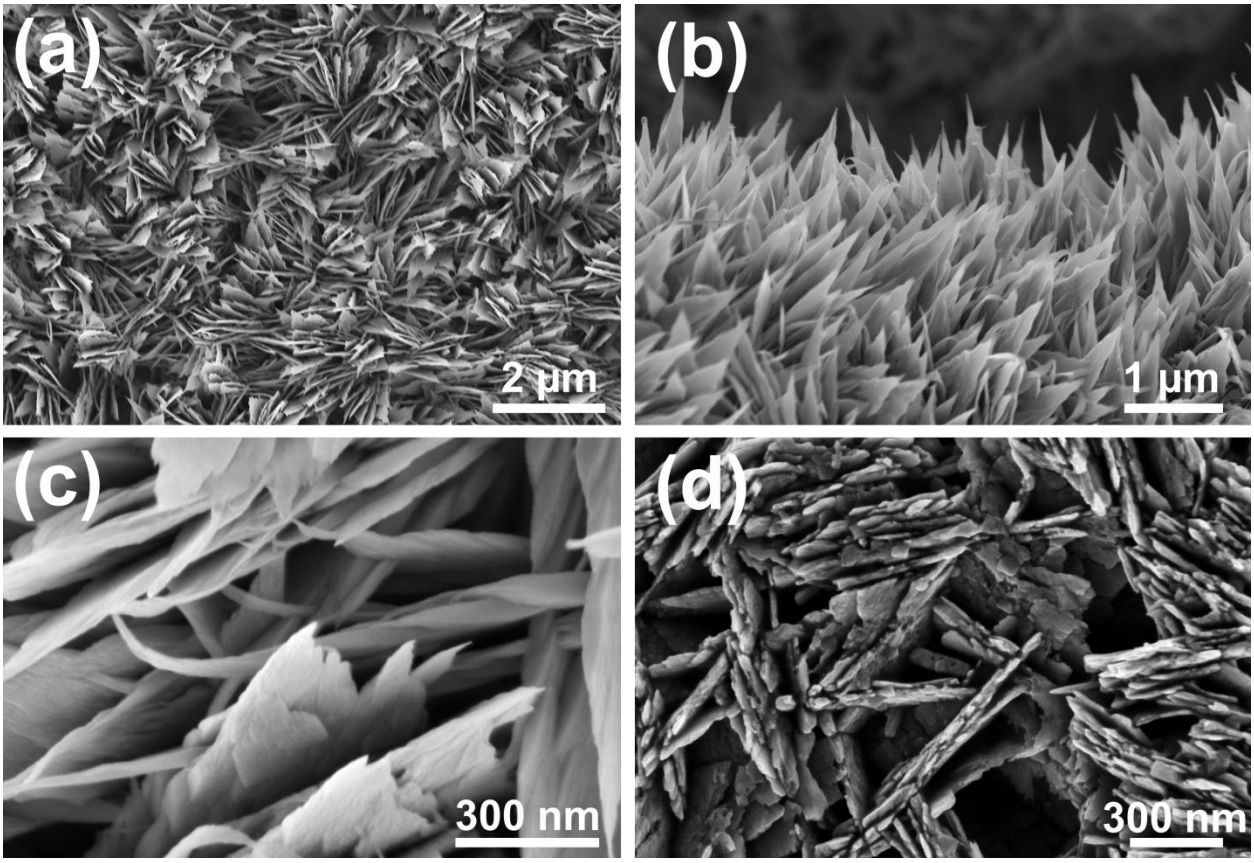


**Figure 1 – Nanostructure characterization.** Field emission scanning electron microscopy (FESEM) images of a 5 minute CuO surface with (a) top view, no silane, (b) side view, no-silane (c) high magnification showing the blade structure of the oxide, no silane, and (d) high magnification after silane deposition. Due to imperfect monolayer formation, silane deposition thickens the oxide blades but maintains the general nanostructure morphology. The sharp, knife-like CuO structures have characteristic heights, $h \approx 1$ μm, solid fraction, $\varphi \approx 0.023$, and roughness factor, $r \approx 10$.

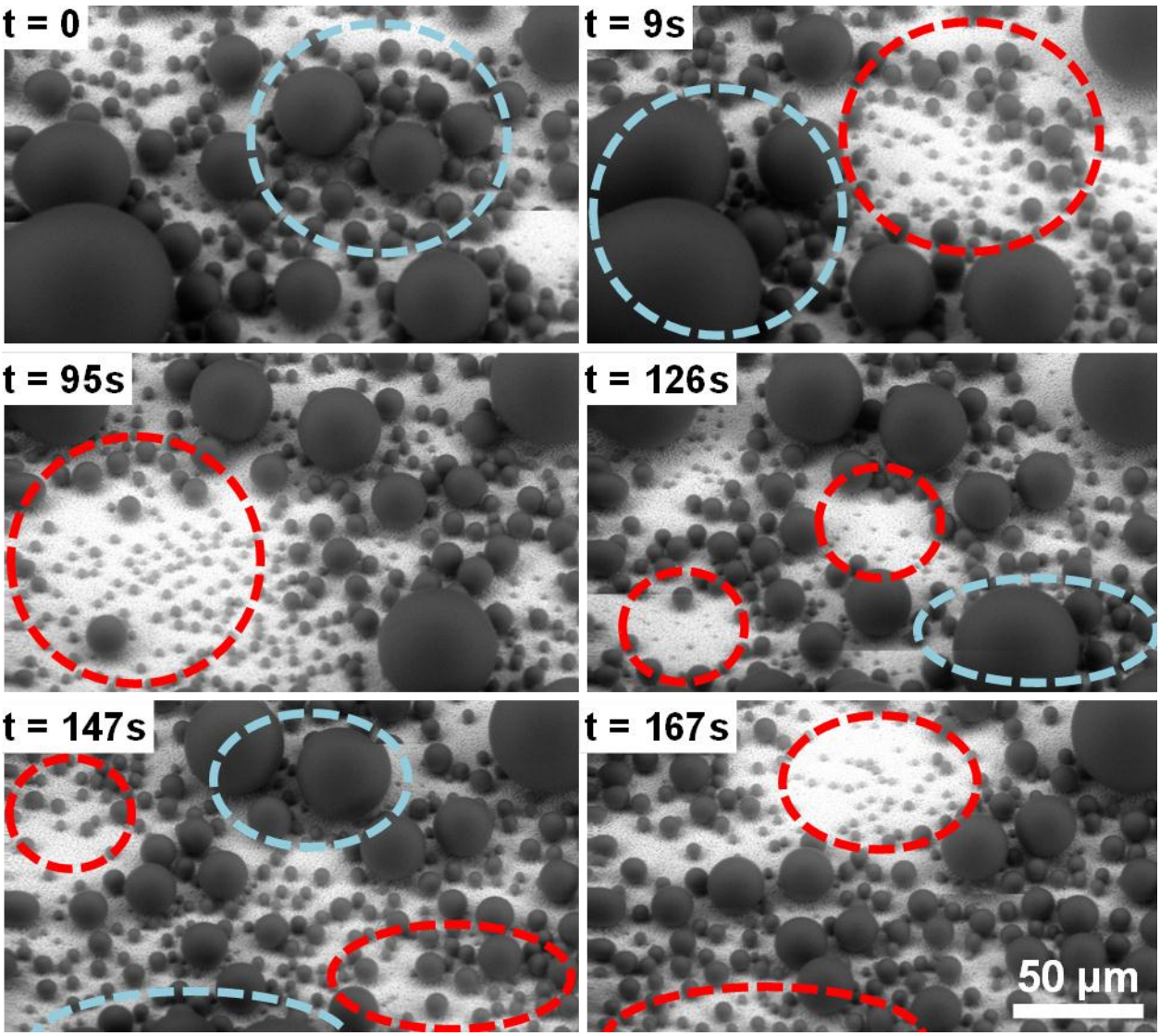


**Figure 2 – Droplet growth dynamics.** Time-lapse images captured *via* environmental scanning electron microscopy (ESEM) of steady state water condensation on a 10 minute CuO surface. A large viewing area was used to avoid electron beam heating effects. Condensing droplets underwent spontaneous droplet jumping and surface renewal. Light blue dotted circles highlight areas of the surface with droplets just prior to coalescence and subsequent jumping, while red dotted circles highlight areas of the surface right after droplet jumping ($P_v$ = 860 ± 43 Pa, $T_s$ = 4.5 ± 1.5 ˚C, $S$ = 1.02, see Supporting Information, videoS1).

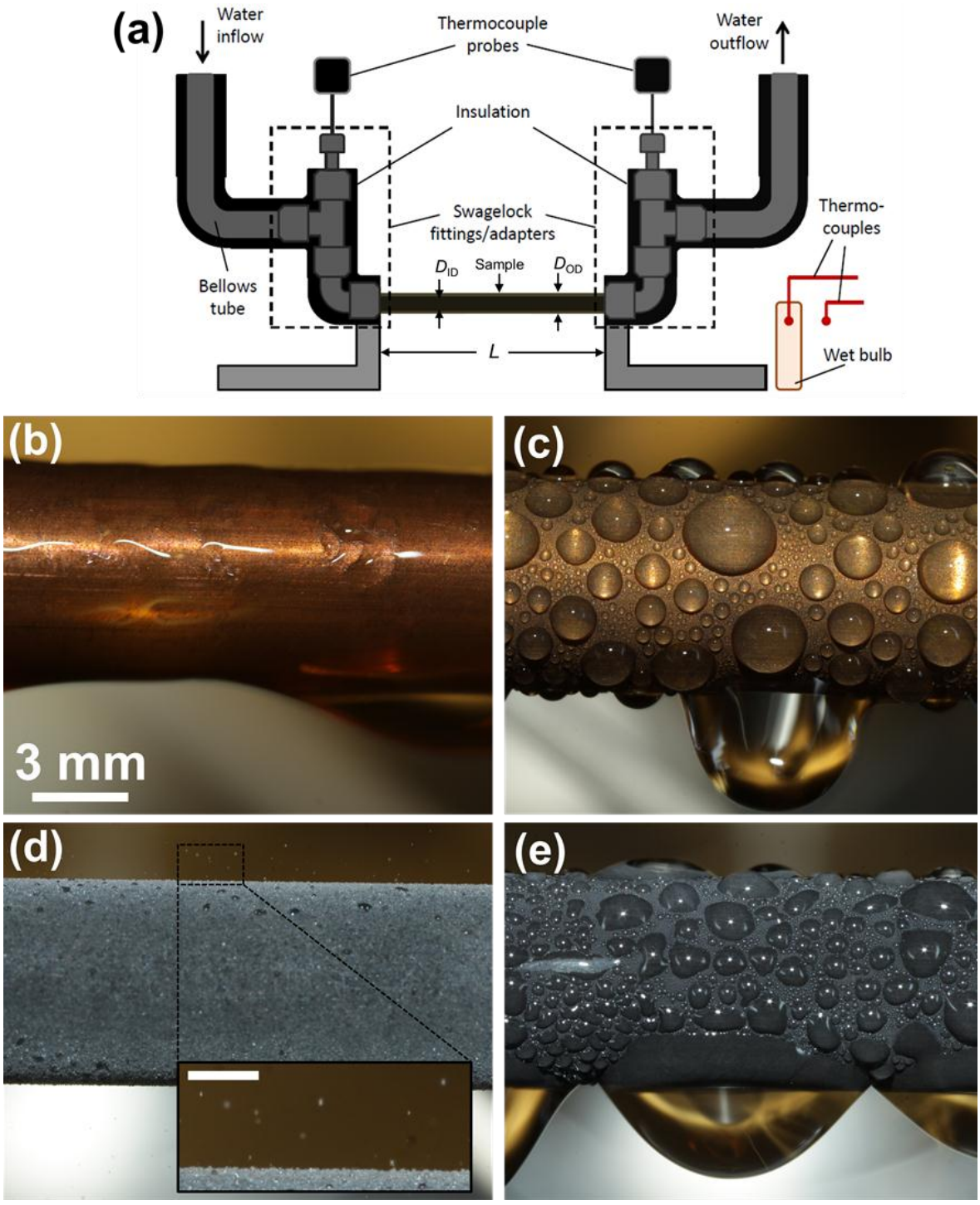


**Figure 3 – Test setup and experimental images of condensation.** (a) Schematic showing experimental setup. The tube sample ($D_{OD}$ = 6.35 mm, $D_{ID}$ = 3.56 mm, $L$ = 131 mm) was cooled *via* chilled water flowing inside the tube at 5 ± 0.1 L/min. Images of (b) filmwise condensation on a smooth hydrophilic Cu tube, (c) dropwise condensation on a silane coated smooth Cu tube, (d) jumping-droplet superhydrophobic condensation on a nanostructured CuO tube (10 minute oxidation) (Inset: magnified view of the jumping phenomena, scale bar is 500 μm), and (d) flooded condensation on a nanostructured CuO tube. The tube dimensions are identical for each case (Chamber vapor pressure $P_v$ = 2700 ± 68 Pa).

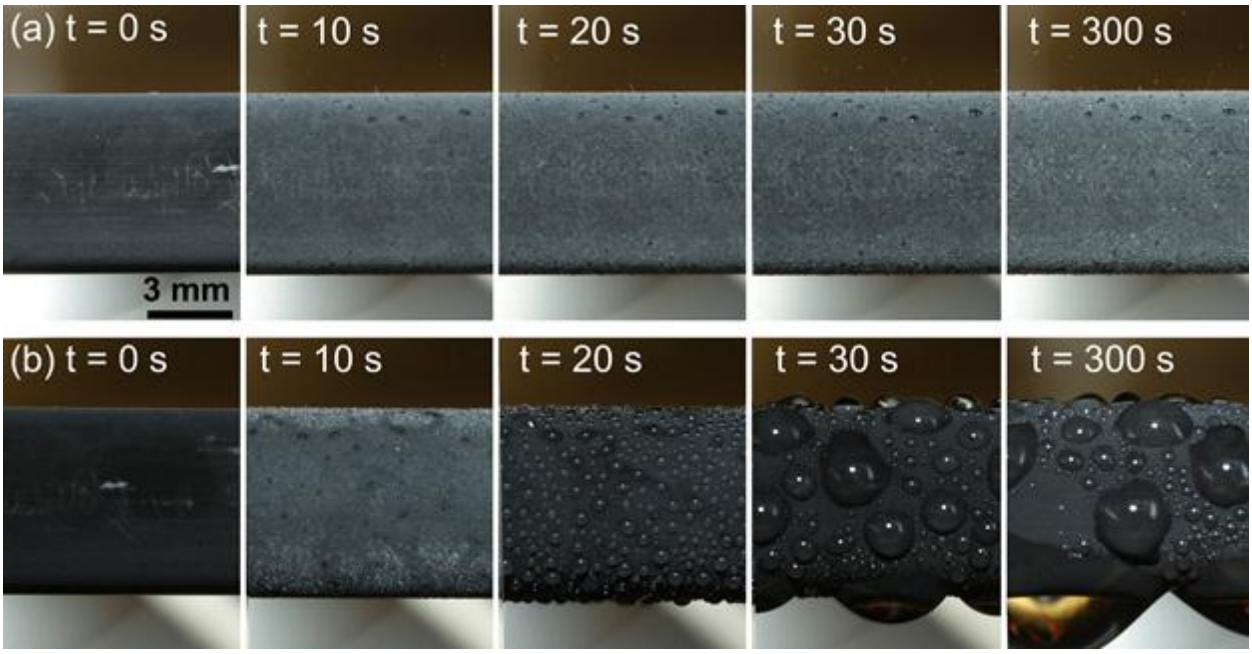


**Figure 4 – Jumping and flooded condensation.** Time-lapse images of initial water condensation on a 10 minute oxidized CuO sample undergoing (a) jumping, ($S$ = 1.08, $\Delta T_{LMTD}$ = 4 K, $P_v$ = 2700 ± 68 Pa) and (b) flooded condensation ($S$ = 1.54, $\Delta T_{LMTD}$ = 12 K, $P_v$ = 2700 ± 68 Pa). Low supersaturations ($S$ = 1.08) led to highly mobile partially wetting droplet formation and subsequent droplet jumping. High supersaturations ($S$ = 1.54) led to surface flooding and the formation of highly pinned Wenzel droplet morphologies.

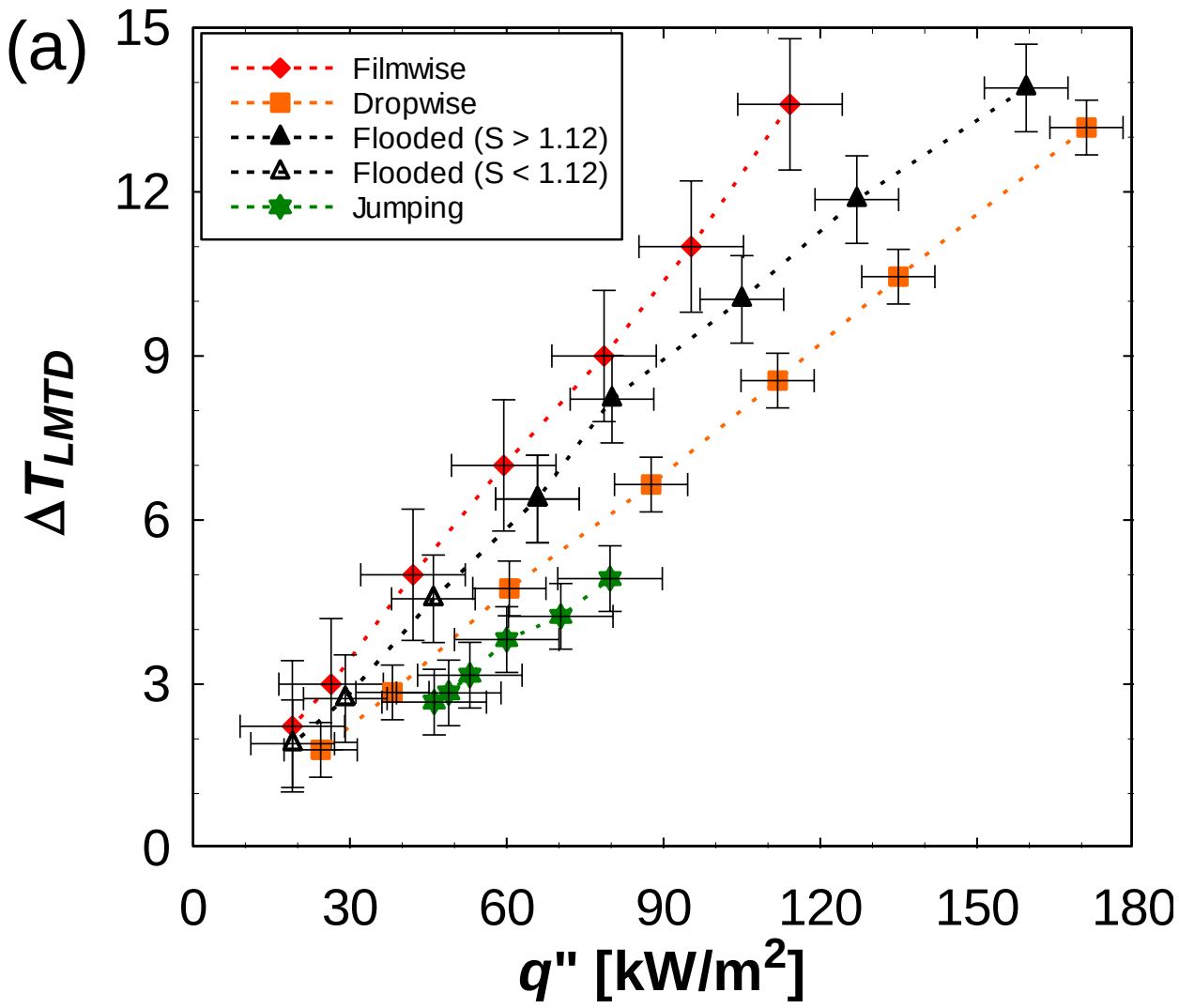
(a)
Filmwise
Dropwise
Flooded (S > 1.12)
Flooded (S < 1.12)
Jumping
ΔT_LMTD
q" [kW/m²]
0
3
6
9
12
15
0
30
60
90
120
150
180

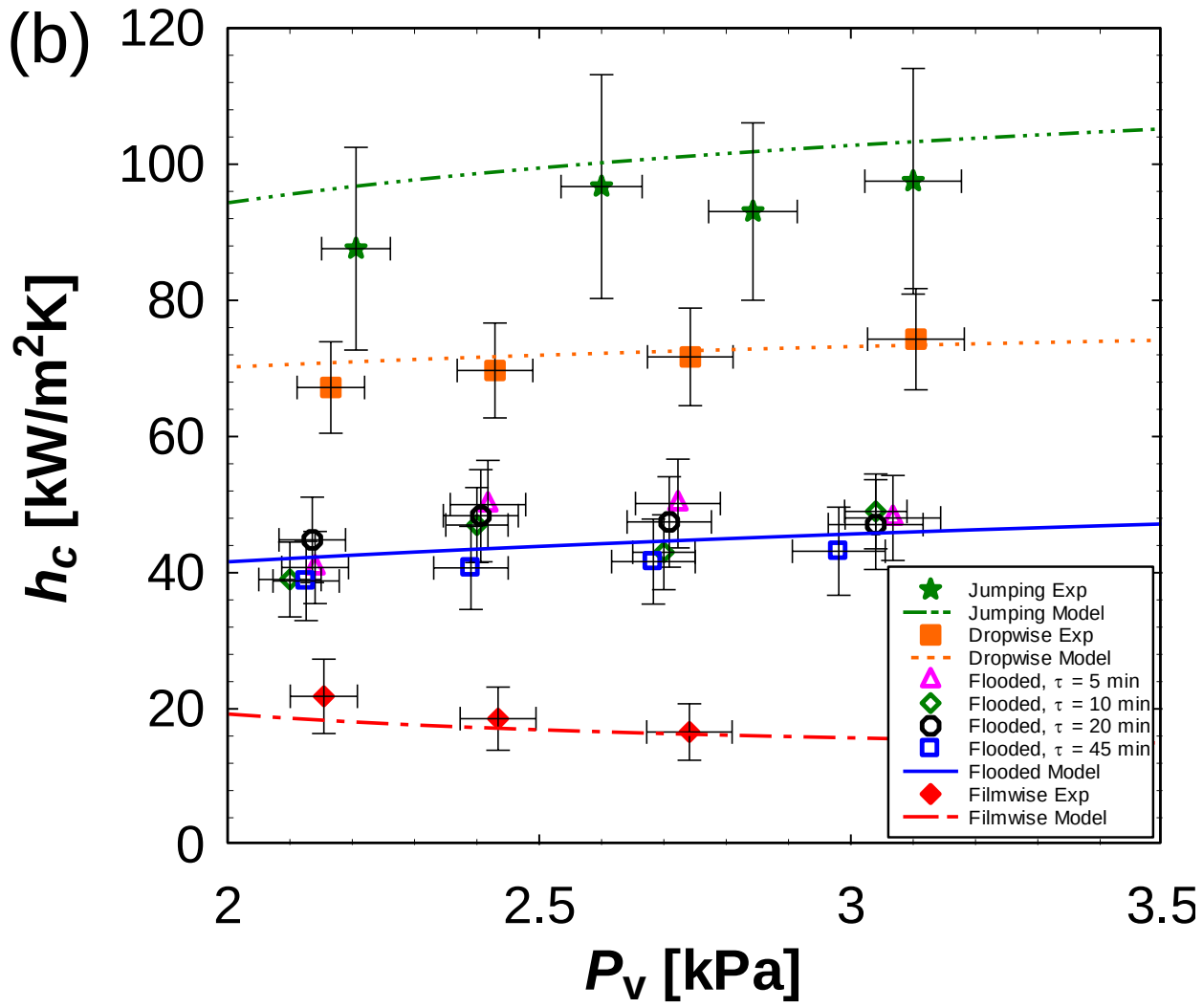


**Figure 5 – Heat transfer performance as a function of supersaturation and vapor pressure.** (a) Experimental steady state log mean water to vapor temperature difference ($\Delta T_{LMTD}$) as a function of overall surface heat flux ($q''$) for tube surfaces undergoing filmwise, dropwise, flooded, and jumping condensation (CuO chemical oxidation time $\tau$ = 10 minutes, chamber vapor pressure $P_v = 2700 \pm 68$ Pa, $1.02 < S \leq 1.6$). Rapid droplet removal due to coalescence induced droplet jumping results in the highest heat fluxes for the jumping sample ($S < 1.12$). However, flooding of the surface at higher heat fluxes results in rapid performance degradation and transition into the flooded condensation mode ($S > 1.12$). Data for the flooded sample at low supersaturations ($S < 1.12$, open triangles) was obtained by flooding the surface and decreasing $\Delta T_{LMTD}$. Due to hysteresis, the jumping behavior was not recovered. (b) Experimental and theoretical steady state condensation coefficient ($h_c$) as a function of saturated vapor pressure ($P_v$) for tube surfaces undergoing filmwise, dropwise, flooded ($\tau$ = 5, 10, 20 and 45 minutes), and jumping ($\tau$ = 10 minutes) condensation (see Supporting Information, section S6). Jumping condensation shows the highest condensation HTC for low supersaturations ($S < 1.12$). Error bars indicate the propagation of error associated with the fluid inlet and outlet temperatures (± 0.2 K) and pressure measurement (± 2.5 %). The jumping surface error bars are the largest due to the relatively low heat fluxes measured ($q'' < 80$ kW/m$^2$), corresponding to the smaller fluid inlet to outlet temperature difference. The theoretical predictions (dotted lines) were obtained from the droplet growth and distribution model (For model derivation and parameters, see Supporting Information, Section S7).

**Table 1 – Sample wetting characteristics.** Silane chemistry, tridecafluoro-1,1,2,2-tetrahydrooctyl)-1-trichlorosilane was used.

| **Sample ID** | **Oxidation Time, τ [minutes]** | **Silanization Time [minutes]** | **Advancing Angle [degrees]** | **Receding Angle [degrees]** |
|---|---|---|---|---|
| Hydrophilic Cu | 0 | 0 | 14.6 ± 6.6 | < 3 |
| Hydrophobic Cu | 0 | 60 | 123.4 ± 2.5 | 81.2 ± 8.4 |
| CuO | 5 | 60 | 169.2 ± 2.6 | 164.1 ± 5.2 |
| CuO | 10 | 60 | 171.2 ± 3.1 | 167.2 ± 3.2 |
| CuO | 20 | 60 | 172.3 ± 2.9 | 168.5 ± 3.1 |
| CuO | 45 | 60 | 172.0 ± 3.2 | 167.8 ± 3.2 |

**TOC GRAPHIC**

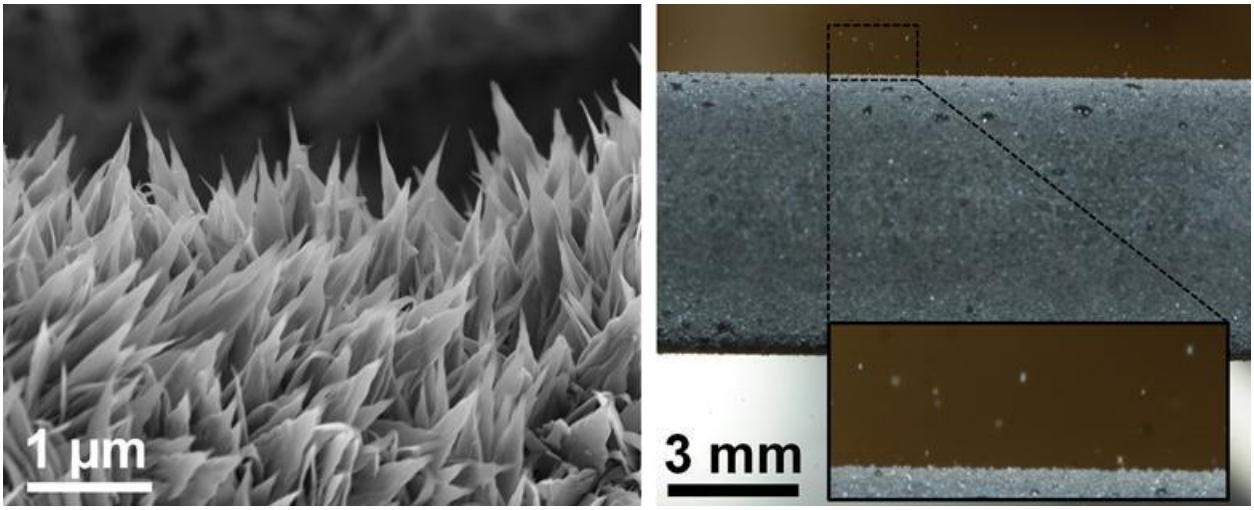

# Supporting Information

## Jumping-Droplet-Enhanced Condensation on Scalable Superhydrophobic Nanostructured Surfaces

Nenad Miljkovic,[1] Ryan Enright,[1,2] Youngsuk Nam,[1,3] Ken Lopez,[1] Nicholas Dou,[1] Jean Sack,[1] and Evelyn N. Wang[1,*]

[1]*Department of Mechanical Engineering, Massachusetts Institute of Technology, 77 Massachusetts Avenue, Cambridge, Massachusetts 02139, USA*
[2]*Stokes Institute, University of Limerick, Limerick, Ireland*
[3]*Kyung Hee University, Yongin, Korea*

*Address correspondence to enwang@mit.edu

### S1. ESEM AND HIGH SPEED VIDEOS

**VideoS1.** Steady state condensation on the flat nanostructured CuO surface captured with an environmental scanning electron microscope, ESEM (Carl Zeiss EVO 50). Droplet removal *via* coalescence-induced ejection was observed once droplets reached a size large enough to begin coalescing. The video was captured at 0.5 fps and is played back at 1 fps. The field of view is 407 μm x 304 μm.

**VideoS2.** Steady state condensation on the clean smooth hydrophilic Cu tube captured with a high speed camera (Phantom v7.1, Vision Research). The tube is oriented in the horizontal direction with cooling water flowing inside the tube at 5 L/min. The vapor pressure is ≈2.7 kPa. A thin liquid water film covers the surface. A droplet slides across the tube due to a small tilt in the tube angle with respect to the horizontal. The video was captured at 90 fps and is played back at 30 fps. The field of view is 160.1 mm x 120.1 mm.

**VideoS3.** Steady state condensation on the smooth hydrophobic Cu tube captured with a high speed camera (Phantom v7.1, Vision Research). The tube is oriented in the horizontal direction with cooling water flowing inside the tube at 5 L/min. The vapor pressure is ≈2.7 kPa. Discrete liquid droplets form on the surface of the tube. Droplets grow and begin to rapidly coalesce with neighboring droplets before being removed by gravity at length scales approaching ≈3 mm. The video was captured at 90 fps and is played back at 90 fps. The field of view is 160.1 mm x 120.1 mm.

**VideoS4.** Steady state condensation on the nanostructured CuO tube captured with a high speed camera (Phantom v7.1, Vision Research). The tube is oriented in the horizontal direction with cooling water flowing inside the tube at 5 L/min. The vapor pressure is ≈2.7 kPa and $\Delta T_{LMTD}$ = 4 K. Droplet removal *via* coalescence-induced ejection occurs once droplets reach sizes large enough to begin coalescing. The video was captured at 90 fps and is played back at 30 fps. The field of view is 160.1 mm x 120.1 mm.

**VideoS5.** Steady state condensation on the nanostructured CuO tube captured with a high speed camera (Phantom v7.1, Vision Research). The tube is oriented in the horizontal direction with cooling water flowing inside the tube at 5 L/min. The vapor pressure is ≈2.7 kPa and $\Delta T_{LMTD}$ = 12 K. Discrete liquid droplets form on the surface of the tube. Droplets grow and begin to rapidly coalesce with neighboring droplets before being removed by gravity at

length scales approaching ≈5 mm. The video was captured at 30 fps and is played back at 30 fps. The field of view is 160.1 mm x 120.1 mm.

## S.2 EXPERIMENTAL SETUP

The custom environmental chamber used for this work (Kurt J. Lesker) consists of a stainless steel frame with a door (sealed with a rubber gasket), two viewing windows, and apertures for various components. Resistive heater lines were wrapped around the exterior of the chamber walls to prevent condensation at the inside walls and then insulated on the exterior walls. The output power of the resistive heater lines was controlled by a voltage regulator (Variac). The chamber temperature was maintained at ≈30˚C for all experiments. Due to the much higher latent heat of vaporization than the water vapor specific heat, a maximum vapor superheating of 5˚C would result in a negligible heat transfer increase of < 0.4%.[1] Two insulated stainless steel water flow lines (Swagelok) were fed into the chamber *via* a KF flange port (Kurt J. Lesker) to supply cooling water to the chamber from a large capacity chiller (System III, Neslab). A flow meter (7 LPM MAX, Hedland) with an accuracy of ± 2% was integrated along the water inflow line.

A secondary stainless steel tube line was fed into the chamber *via* a KF adapter port that served as the flow line for the incoming water vapor supplied from a heated steel water reservoir. The vapor line was wrapped with a rope heater (60 W, Omega) and controlled by a power supply (Agilent). The vapor reservoir was wrapped with another independently-controlled rope heater (120 W, Omega) and insulated to limit heat losses to the environment. The access tubes were welded to the vapor reservoir, each with independently-controlled valves. The first valve (Diaphragm Type, Swagelok), connecting the bottom of the reservoir to the ambient, was used to fill the reservoir with water. The second valve (BK-60, Swagelok), connecting the top of the reservoir to the inside of the chamber, provided a path for vapor inflow. K-type thermocouples were located along the length of the water vapor reservoir to monitor temperature.

A bellows valve (Kurt J. Lesker) was attached to the chamber to serve as a leak port between the ambient and inside of the chamber. In order to monitor temperatures within the chamber, K-type thermocouple bundles were connected through the chamber apertures *via* a thermocouple feed through (Kurt J. Lesker). A pressure transducer (925 Micro Pirani, MKS) was attached to monitor pressure within the chamber. The thermocouple bundles and the pressure transducer were both electrically connected to an analog input source (RAQ DAQ, National Instruments), which was interfaced to a computer for data recording. A second bellows valve (Kurt J. Lesker) was integrated onto the chamber for the vacuum pump, which brought down the chamber to vacuum conditions prior to vapor filling. A liquid nitrogen cold trap was incorporated along the line from the chamber to the vacuum which served to remove any moisture from the pump-down process and ultimately assist in yielding higher quality vacuum conditions. A tertiary bellows valve (Kurt J. Lesker) was integrated on a T fitting between the vacuum pump and liquid nitrogen reservoir to connect the vacuum line to the ambient to release the vacuum line to ambient conditions once pump down was achieved. In order to visually record data, a high speed camera (Phantom v7.1, Vision Research) was placed in line with the 5” viewing windows on the chamber. In addition, a digital SLR camera (Cannon) was

interchangeable with the high speed camera to obtain color images. The schematic of the exterior of the environmental setup is depicted in Figure S1a. Photographs of the front and rear of the experimental setup are shown in Figures S1b and c, respectively.

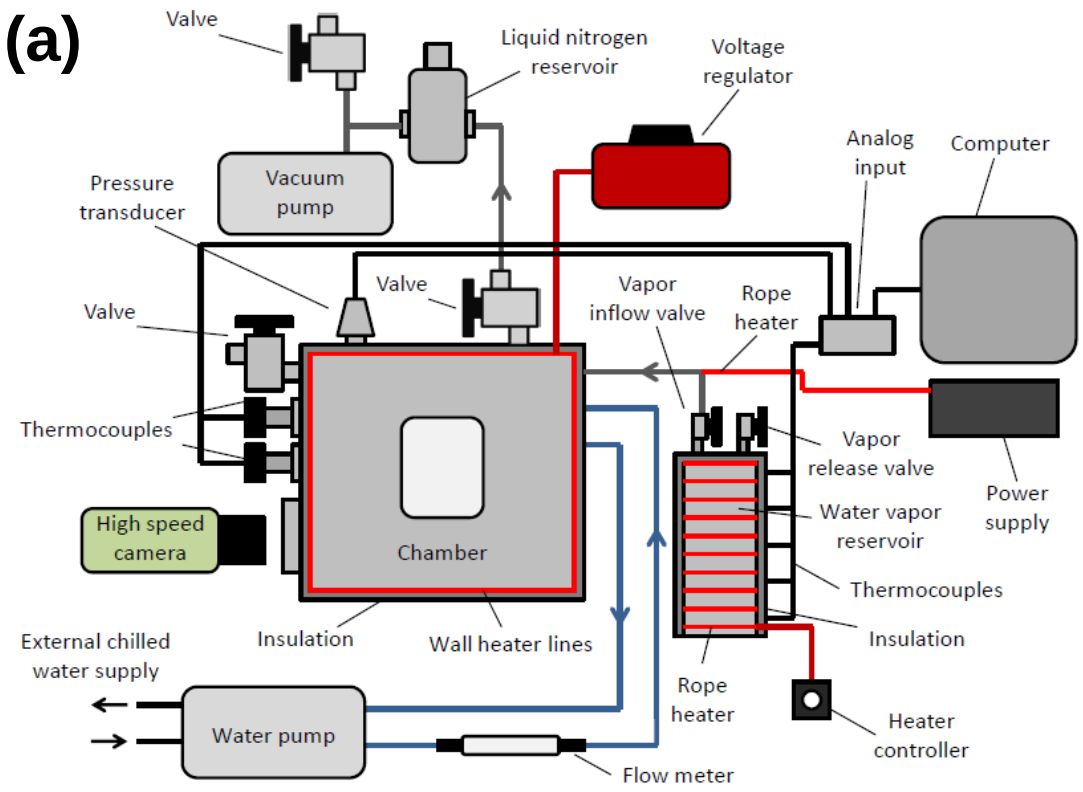

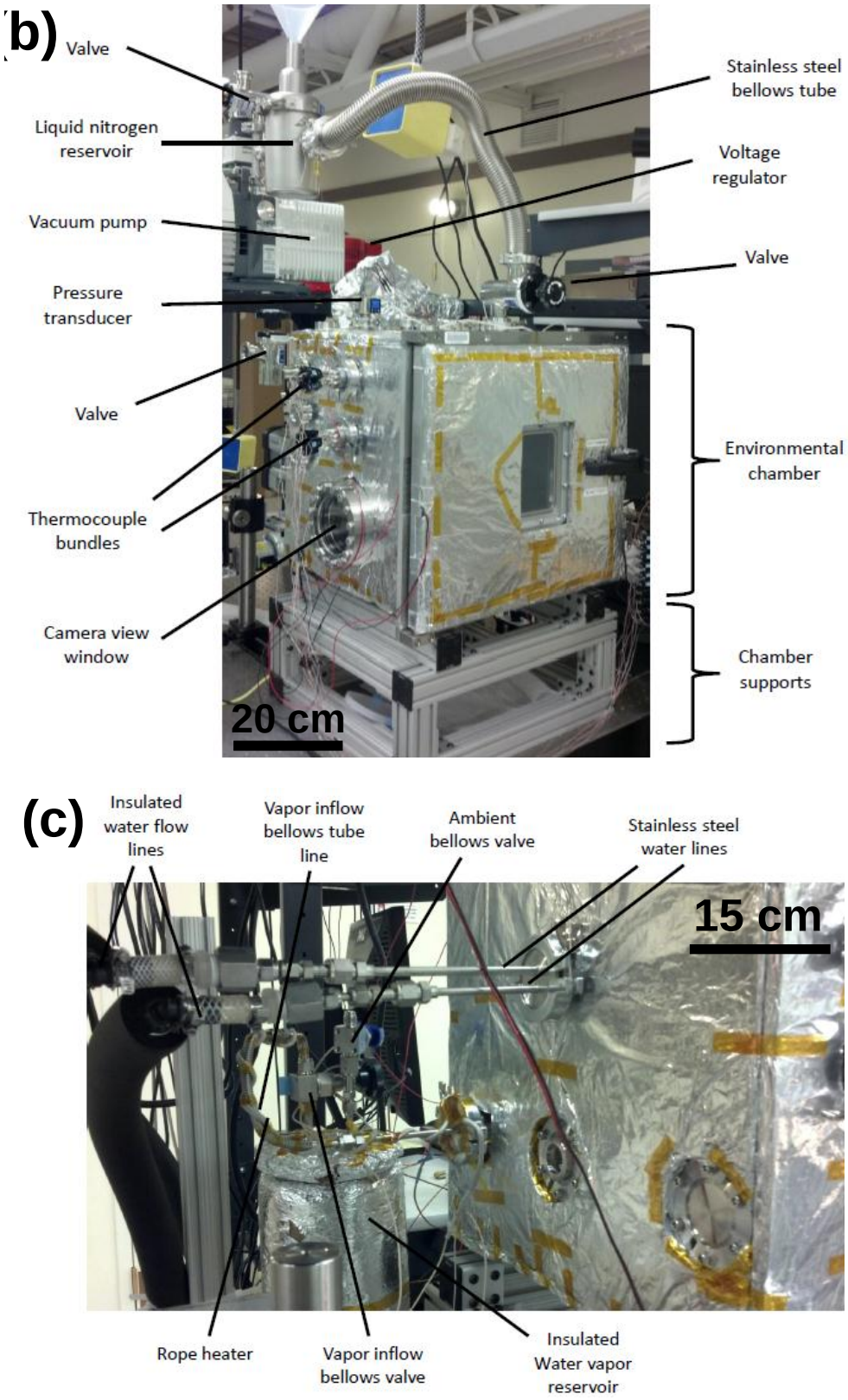


**Figure S1 –** (a) Schematic of experimental setup (not to scale). (b) Photograph of the experimental setup shown from the front (high speed camera and data acquisition system not shown). (c) Photograph of the experimental setup from the rear of the chamber showing the cooling water inlet and outlet and water vapor reservoir.

The setup used to run experiments inside the chamber is shown in Figure S2. Stainless steel bellows tube lines (1/4", Swagelok) were connected to the external water flow lines (Figure S1c). T-connection adapters (Swagelok) with bore through Ultra-Torr fittings (Swagelok) were used to adapt K-type thermocouple probes (Omega) at the water inlet and outlet. Prior to experimentation, the thermocouple probes were calibrated using a high precision temperature controlled bath (Lauda Brinkman) to an accuracy of ± 0.2 K.

The test samples, 6.35 mm diameter tubes with different surface treatments, were connected *via* a Swagelok compression fitting onto the T-connection. Chilled water flows through the inlet bellows tube, along the inside of the tube sample and through the outlet. Two supports were used to hold the sample and the entire configuration in place. Two separate pieces of insulation were embedded with K-type thermocouple leads and used for wet bulb temperature measurement during experimental runs. A third thermocouple was placed beside the sample to measure the reference temperature inside the chamber. As the experiment progressed, the wet-bulb insulating wick collected water from the bottom of the chamber to the embedded thermocouple. The temperature measured by this thermocouple was compared to the reference temperature calculated from the saturation pressure. This allowed for a high accuracy secondary measurement of saturation conditions inside the chamber.

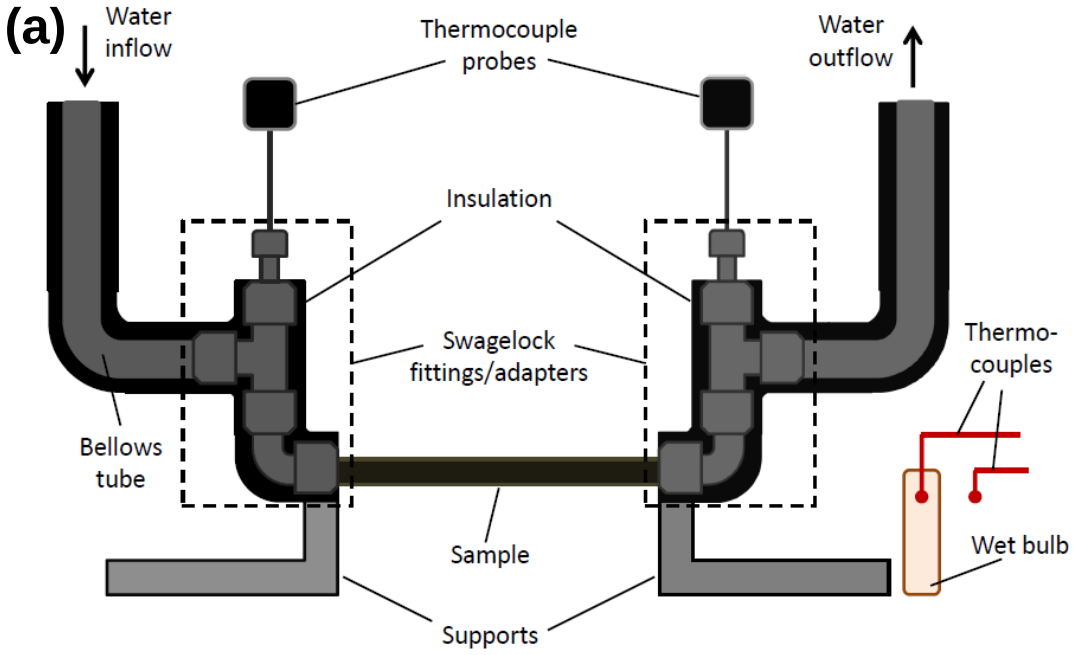

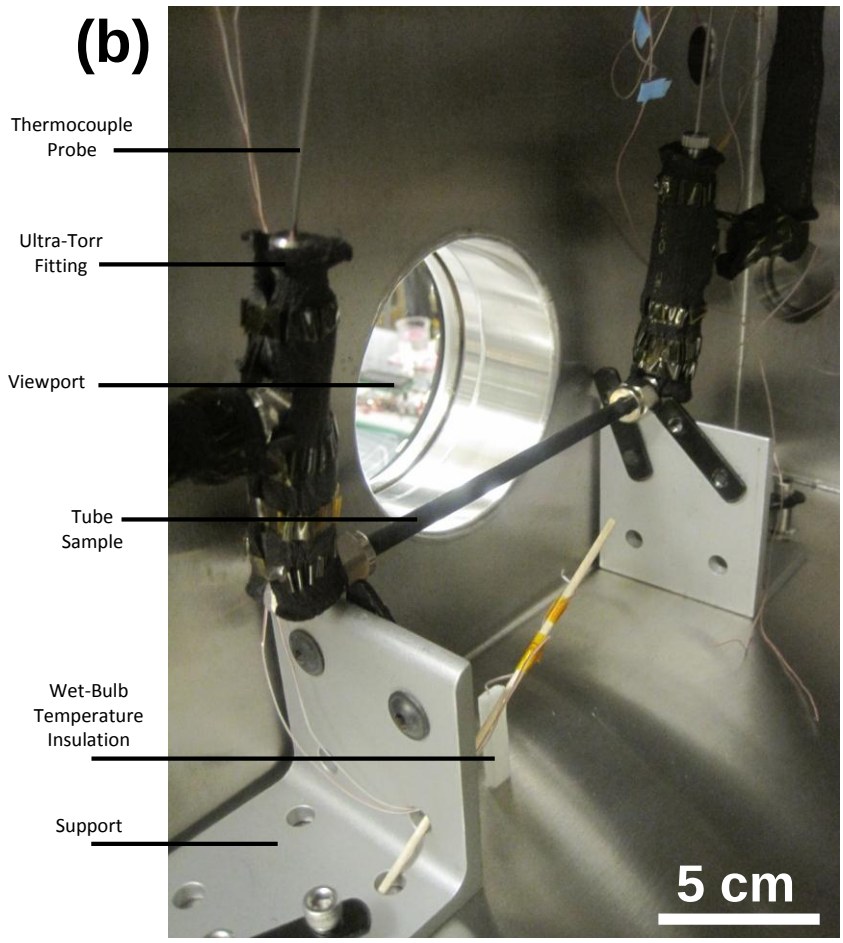


**Figure S2 –** (a) Schematic of experimental setup inside the chamber (not to scale). (b) Photograph of the experimental setup inside the chamber showing a CuO nanostructured tube in place for testing.

## S.3 EXPERIMENTAL PROCEDURE

For each experimental trial, a set of strict procedures were followed to ensure consistency throughout the experiments. The first step of the process was to turn on the voltage regulator to heat up the environmental chamber walls, which prevented condensation inside the chamber walls. Simultaneously, the water vapor reservoir was filled with approximately 3.5 liters of DI water (99% full) using a syringe through the vapor release valve. After opening the vapor inflow valve and closing the vapor release valve, the rope heater around the water vapor reservoir was turned on with the heater controller set to maximum output. Then the rope heater connected to the vapor inflow valve was turned on. The temperature of the water reservoir was monitored with the installed thermocouples; the temperature at the top of the reservoir was higher than that of the middle/bottom of the reservoir due to the water thermal-mass present at the middle/bottom section. Hence, we ensured that the regions of the water reservoir of higher thermal capacity were brought to a sufficiently high temperature for boiling. During the boiling process, aluminum foil was placed on the bottom surface of the inner chamber to collect any of the water leaving the vapor inflow line. Once boiling was achieved and all thermocouples on the reservoir were > 95˚C for at least 10 minutes,

the vapor inflow valve was closed. The excess water that spilled inside the chamber during de-gassing of the reservoir was removed.

In order to install the samples onto the rig (Figure S2), the Swagelok female adapters at the ends of the tube samples were connected to the 90 degree male elbow connecters on the rig. Before installing the entire sample setup in the chamber, all adapters/connecters were tightened to ensure that there were no leaks that could affect vacuum performance. The setup was then placed on top of the steel supports and the bellows tubes (for the water inflow/outflow) were connected to the water lines. Then the insulating wet bulb wick was placed near the sample and in contact with the bottom surface of the chamber.

The next step was to begin the vacuum pump-down procedure. Initially, the liquid nitrogen cold trap was filled to about half capacity. The ambient exposed valves connecting the chamber and the vacuum pump were both closed and the valve connected to the liquid nitrogen cold trap was opened. The vacuum pump was then turned on, initiating the pump-down process. The pressure inside the chamber was monitored during the pump-down process (Figure S3). This process took approximately one hour in order to achieve the target vacuum conditions ($0.5\ Pa < P < 1\ Pa$). The experimental operating pressure of non-condensable was set to be a maximum of 0.25% of the operating pressure. Non-condensable gas content of above 0.5% (pressure) was shown to significantly degrade performance during dropwise condensation.[2, 3] In our experiments, extreme care was taken to properly de-gas the vacuum chamber and water vapor reservoir prior to experimental testing. In addition, the chamber leak rate was characterized prior to each run in order to estimate the maximum time available for acquiring high fidelity data with non-condensable content of less than 0.25%.

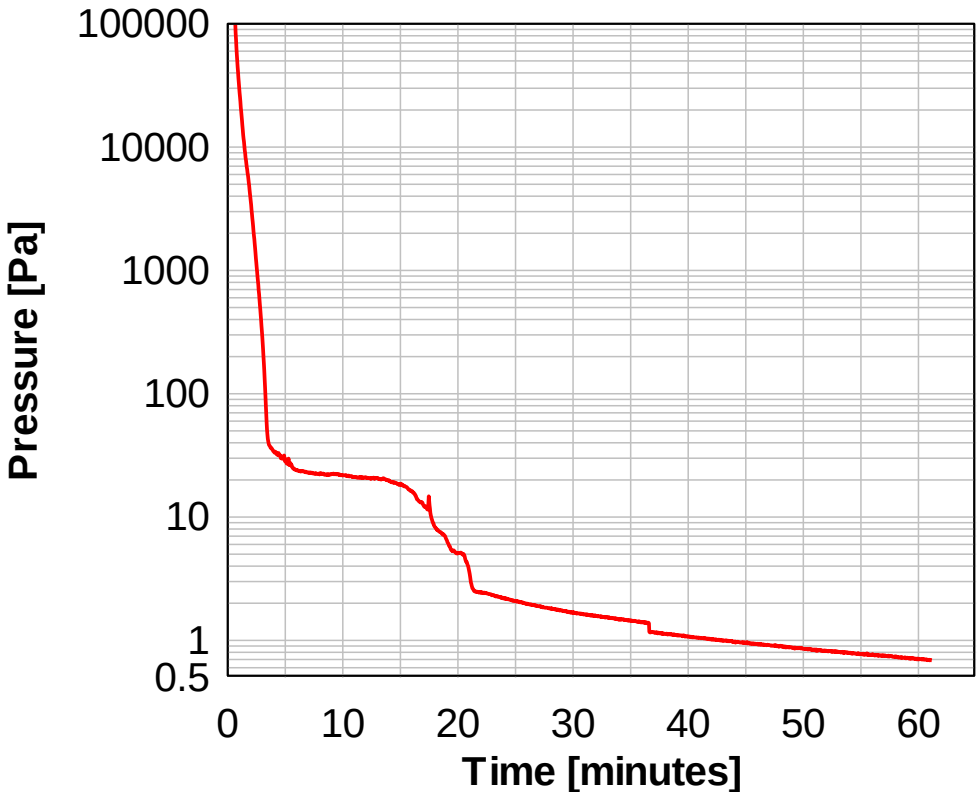


**Figure S3 –** Chamber pressure as a function of time during a typical pump down operation. The kinks in the data were due to evacuation of water vapor and ice left over in the chamber from a previous experimental run.

The setup of the water flow-loop is described as follows. The Neslab water pump reservoir was filled and turned on to a flow rate of 5 L/min ($0 < \Delta T_{LMTD} < 15$ K). The flow rate was monitored with the flow meter integrated in the inflow water line. In order to bring the chilled water into the flow loop and to the tube sample, the external chilled water lines were opened. The relatively high flow rate of 5 L/min was chosen to maximize the internal water heat transfer coefficient and therefore reduce the total condenser thermal resistance.

Prior to beginning experiments, the high-speed camera was turned on for visual recording of the sample during condensation. Afterwards, the rope heater around the water reservoir was turned off and the vapor inflow valve was slowly turned open until the operating pressure was reached. Steady state conditions were typically reached after 2 minutes of full operation. Once at steady state, data was recorded over a 10 minute interval. After the data was recorded, the pressure level was increased or decreased to a new level by opening or closing the vapor inflow valve.

## S.4 FABRICATION DETAILS

Tube Cleaning Procedure

Experimental Cu tube samples were rigorously cleaned in a systematic manner prior to testing. All tubes were interfaced with a female ¼" Swagelok fitting on each end and capped with a ¼" Swagelok nut. Capping of the tubes ensured that no oxidation or functionalization occurred inside the tube to keep the same cooling water flow conditions. Once capped, the tubes were cleaned in an ultrasonic bath with acetone for ≈10 minutes at room

temperature. The tubes were then rinsed with ethanol, isopropyl alcohol (IPA) and de-ionized water (34877, Sigma) (Figure S4). The tubes were then dried in a clean nitrogen stream and immediately dipped into a 2.0 M hydrochloric acid solution for 10 minutes to remove the native oxide film on the surface. Once complete, the tubes were removed from the HCl bath and vigorously triple-rinsed with DI water, and dried with a clean nitrogen stream.

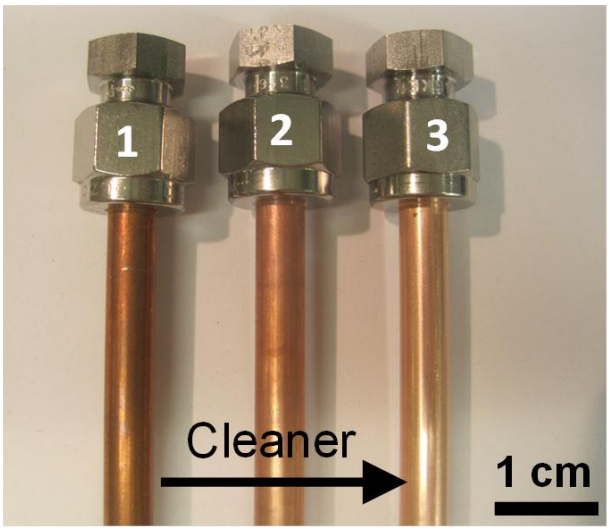


**Figure S4 –** Images of smooth Cu test tubes during the cleaning process: (1) as-is Cu tube (not cleaned), (2) cleaned Cu tube using solvents (acetone, IPA, water rinse), (3) cleaned Cu tube after 2M HCl step to remove oxide.

To study the fabricated tube surface morphology using FESEM, additional flat and small tube samples (Figure S5) were fabricated during creation of the large tube test samples. After cleaning, the samples had a visibly brighter color.

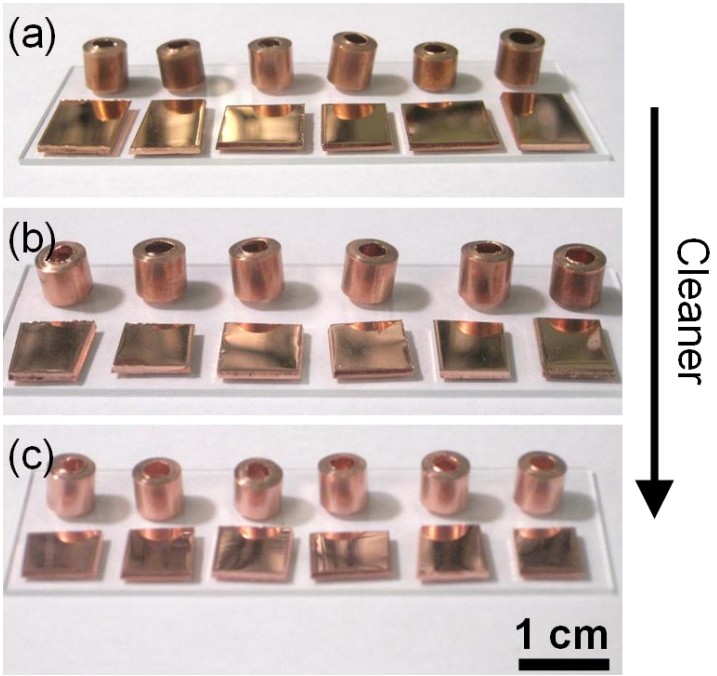


**Figure S5 –** Smooth Cu test sections with Cu plates during cleaning process (a) as-is Cu (not cleaned), (b) cleaned Cu using solvents (acetone, IPA, water rinse), (c) cleaned Cu tube after 2M HCl step to remove oxide.

Silane Deposition

The nanostructured CuO and smooth Cu tubes were functionalized using chemical vapor deposition of a fluorinated silane (trichloro(1H,1H,2H,2H-perfluorooctyl)silane, Sigma). Prior to silane deposition, each tube was oxygen plasma cleaned for 2 hours to remove organic contaminants on the surface. Once clean, the tube samples were immediately placed in a vacuum desiccator (06514-10, Cole Parmer) with a small amount of liquid silane. The desiccator was evacuated by a roughing pump for 30 minutes to a minimum pressure of ≈10 kPa. A valve was then closed to isolate the pump from the desiccator and the sample was held in vacuum (≈10 kPa) for another 30 minutes. The silanated tubes were then rinsed in ethanol and DI water, and dried in a clean nitrogen stream. It is important to note, the long plasma cleaning time creates heating of the sample and raises the sample temperatures to ≈60˚C. The higher temperature is beneficial during vapor phase deposition of the silane due to the higher silane-substrate bond formation at elevated temperatures.[4]

## S.5 SURFACE CHARACTERIZATION

Oxide Thickness

To characterize the oxide thickness of the tested samples (smooth and nanostructured), we used focused ion beam milling (FIB) (NVision 40 Dual Beam Focused Ion Beam, Carl Zeiss GMBH) and SEM imaging. Milling was performed with normal incidence of the ion beam (sample tilt of 54˚), ion beam energy of 30 keV, and ion current of 300 pA. The structure cross-sections were obtained by milling 8 μm deep x 20 μm wide trenches. Due to the good milling response of copper, surface polishing was not required. All samples were imaged at 36˚ tilt using the in lens detector with electron beam energies of 7 keV.

The $Cu_2O$ oxide thicknesses for both the smooth (hydrophobic and hydrophilic) and nanostructured samples were ≈300 nm (Figure S6). With the additional CuO blades on the nanostructured samples, however, the total copper oxide thickness was ≈1.5 μm (Figure S6c,d), as expected.[5-7] It is important to note, Figures S6a,b show the presence of grain boundaries beneath the oxide film. These grain boundaries should not be mistaken for the $Cu_2O$ oxide layer, which exists only adjacent to the surface of the sample as indicated by the arrows.

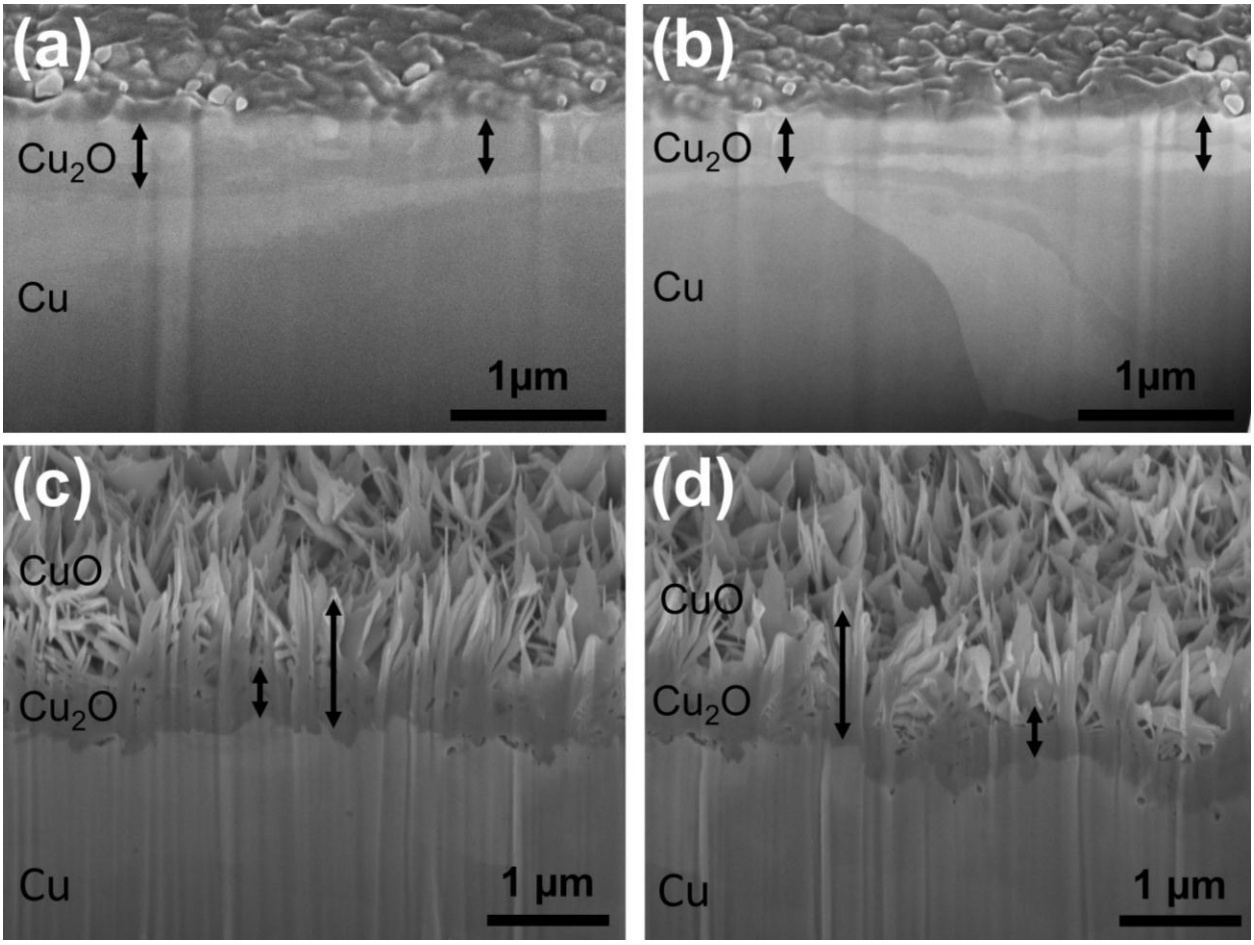


**Figure S6 –** SEM images of FIB milled samples showing the a-b) smooth hydrophobic and hydrophilic sample oxide thickness and c-d) 10 minute oxidized CuO nanostructured sample thickness. The smooth sample $Cu_2O$ thickness was ≈300 nm while the nanostructured $Cu_2O$ + CuO layer was ≈1.5 µm thick with a ≈300 nm thick $Cu_2O$ layer. Images a) and b) were obtained on two separate FIB milled spots, as were images c) and d).

Contact Angle Measurements

To test the wetting characteristics of the fabricated samples, micro-goniometric measurements (MCA-3, Kyowa Interface Science Co., Japan) on each fabricated sample were obtained (Figure S7).

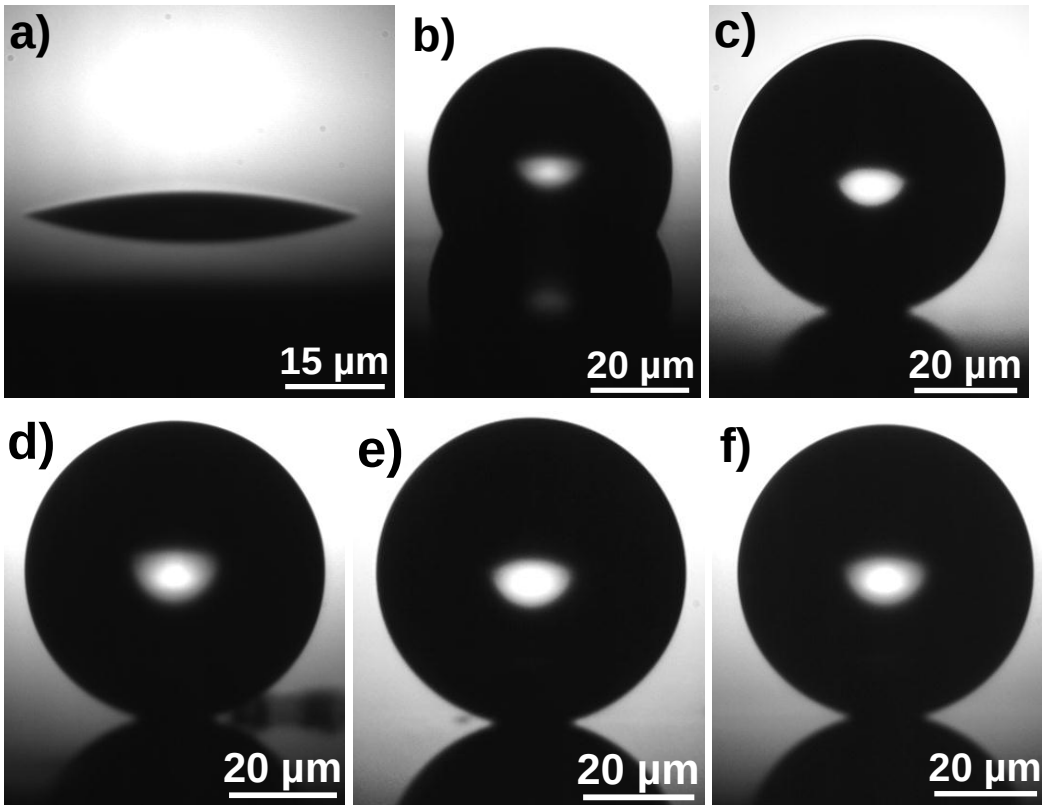


**Figure S7 –** Micro-goniometer contact angle measurement images of a) smooth hydrophilic Cu, b) smooth hydrophobic Cu, c) 5 minute oxidized CuO, d) 10 minute oxidized CuO, e) 20 minute oxidized CuO and f) 45 minute oxidized CuO. The images represent the advancing contact angles for each case. Refer to Table 1 for contact angle measurement data.

ESEM Imaging Procedure

Condensation nucleation and growth were studied on these fabricated surfaces using an environmental scanning electron microscope (EVO 55 ESEM, Carl Zeiss GMBH). Backscatter detection mode was used with a high gain. The water vapor pressure in the ESEM chamber was 800 ± 80 Pa. Typical image capture was obtained with a beam potential of 20 kV and variable probe current depending on the stage inclination angle. To limit droplet heating effects, probe currents were maintained below 2.0 nA and the view area was kept above 400 µm × 300 µm. A 500 µm lower aperture was used in series with a 100 µm variable pressure upper aperture to obtain greater detail. The sample temperature was initially set to 4 ± 1.5 °C and was allowed to equilibrate for 5 minutes. The surface temperature was subsequently decreased to 3 ± 1.5 °C, resulting in nucleation of water droplets on the sample surface. Images and recordings were obtained at an inclination angle of 45° from the horizontal to observe droplet jumping. Cu tape was used for mounting the sample to the cold stage to ensure good thermal contact.

Droplet Size Distribution

To determine the mean coalescence length for condensed droplets on the CuO nanostructures, the droplet size distribution was obtained from the ESEM images. Droplet number density and size were measured from multiple images of the steady-state condensation process, accounting for inclination angle (Figure S8). As a result of the high

nucleation density, $N \approx 5\text{x}10^9$ m$^{-2}$, the mean center-to-center spacing of the droplets was ≈8 μm and coalescence-induced jumping maintained droplet sizes below 10 μm.

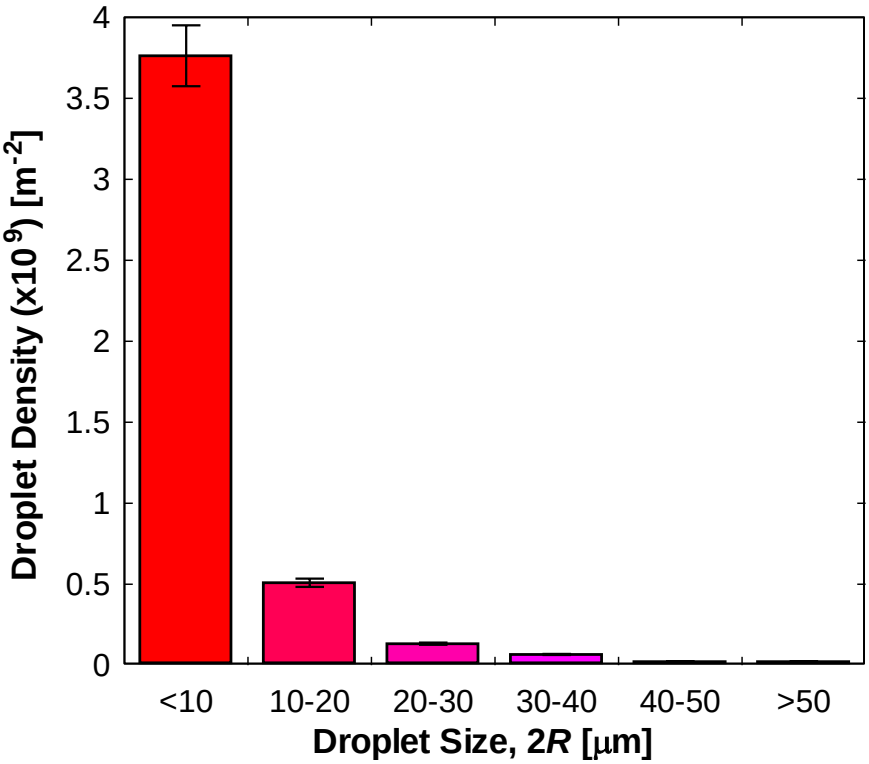


**Figure S8** - Droplet size distribution for steady state condensation at a supersaturation S ≈ 1.1. The counting error associated with the droplet distribution measurements from the ESEM images was estimated to be ≈5% at each size range.

## S.6 EXPERIMENTAL CALCULATIONS

Overall Heat Transfer Coefficient ($\bar{U}$)

To calculate the condensation heat transfer, the energy applied to the tube sample was balanced by the change in enthalpy of the cooling fluid:

$$Q = \dot{m} c_p (T_{out} - T_{in}) \,, \tag{S1}$$

where $Q$ is the total condensation heat transfer rate, $\dot{m}$ is the cooling water mass flow rate inside the tube, $c_p$ is the liquid water specific heat, and $T_{out}$ and $T_{in}$ are the tube outlet and inlet temperatures, respectively. To obtain the overall heat transfer coefficient, $\bar{U}$ from the experiment, the measured heat transfer rate ($Q$) was equated to an equivalent form with the overall heat tranfer coefficient:

$$\dot{m} C_p (T_{out} - T_{in}) = \bar{U} A \Delta T_{LMTD} \,, \tag{S2}$$

where $A$ is the tube outer surface area ($A = \pi d_{OD} L$) and $\Delta T_{LMTD}$ the log mean temperature difference (LMTD) defined by[8]:

$$\Delta T_{LMTD} = \frac{(T_v - T_{in}) - (T_v - T_{out})}{\ln\left(\frac{T_v - T_{in}}{T_v - T_{out}}\right)}. \quad \text{(S3)}$$

The overall heat transfer coefficient is therefore

$$\overline{U} = \frac{\dot{m} C_p (T_{out} - T_{in})}{A \Delta T_{LMTD}}, \quad \text{(S4)}$$

which is only a function of experimentally measured parameters.

Condensation Heat Transfer Coefficient ($h_c$)

The previously calculated $\bar{U}$ is a measure of the overall heat transfer performance from the vapor to cooling water. This approach allows for a fair surface comparison since all of the thermal resistances in the heat transfer network were considered including the temperature drop through the oxide layer, Cu tube, and convection heat transfer coefficient to the cooling water flow. However, to quantify the *condensation* heat transfer coefficient, $h_c$, (as measured from the vapor to the tube outer surface), further calculations were performed.

To extract $h_c$, the overall surface heat flux was used in combination with the forced convection cooling water flow heat transfer coefficient and the tube radial temperature drop to calculate the outer surface temperature. To determine the forced convection internal flow heat transfer coefficient, the Gnielinski correlation was used which has been shown to have an accuracy of ± 5%:[8]

$$h_i = \frac{k_i}{d_{ID}} \frac{\left(\frac{f}{8}\right)(Re - 1000)Pr}{1 + 12.7\left(\frac{f}{8}\right)^{\frac{1}{2}}(Pr^{\frac{2}{3}} - 1)}, \quad \text{(S5)}$$

$$Re = \frac{\rho v d_{ID}}{\mu}, \quad \text{(S6)}$$

$$f = (0.790 \ln Re - 1.64)^{-2}, \quad \text{(S7)}$$

where $h_i$ is the internal cooling water flow heat transfer coefficient, $f$ is the pipe friction factor, $Re$ is the cooling water flow Reynolds number, $Pr$ is the Prandtl number, $\rho$ is the cooling water density, $k_i$ is the cooling water thermal conductivity, and $\mu$ is the cooling water dynamic viscosity.

With $h_i$ determined, a closed form solution can be obtained for $h_c$ by combining all of the relevant temperature drops (internal cooling water flow, radial conduction through the Cu tube, and radial conduction through the oxide):[9, 10]

$$h_c = \left( \frac{1}{\overline{U}} - \frac{A}{A_i h_i} - \frac{A \ln\left(\frac{d_{OD}}{d_{ID}}\right)}{2\pi L k_{Cu}} \right)^{-1}, \quad \text{(S8)}$$

where $A$ is the tube outter surface area ($A = \pi d_{OD} L$), $A_i$ is the internal tube surface area ($A_i = \pi d_{ID} L$), $L$ is the tube sample length, and $k_{Cu}$ is the Cu thermal conductivity ($k_{Cu}$ = 401 W/mK). Note in this case, the $Cu_2O$ layers in the samples are comparable (≈300 nm). While the nanostructure samples have additional CuO blades, because the droplets form in the partially wetting droplet morphology,[11] the CuO blades do not contribute as an added thermal resistance. For completeness, we also determined the temperature drop across the $Cu_2O$ layer. Since the $Cu_2O$ layer in both cases are thin (≈300 nm), and that the $Cu_2O$ has a relatively high thermal conductivity (≈20 W/mK)[12] when compared to typical functional coatings (≈0.2 W/mK)[13, 14], the temperature drop across this layer is small. We calculated the temperature drop in the case of maximum heat flux prior to flooding (≈8 W/cm$^2$) for the jumping nanostructured surface as $\Delta T_{oxide} \approx q'' t_{oxide}/k_{oxide} \approx$ (8 W/cm$^2$)(300x10$^{-7}$cm) / (0.2 W/cmK) ≤ 0.0012 K, where $\Delta T_{oxide}$ is the temperature drop across the oxide layer, $q''$ is the heat flux (≈8 W/cm$^2$), toxide is the $Cu_2O$ oxide layer thickness (≈300 nm), $k_{oxide}$ is the $Cu_2O$ oxide layer thermal conductivity (≈20 W/mK)[12].

## S.7 MODEL

For the model, $h_c$ was obtained by incorporating the individual droplet heat transfer with droplet size distribution:[11, 15]

$$h_c = \frac{q''}{\Delta T} = \frac{1}{\Delta T}\left[\int_{R^*}^{R_e} q(R) n(R) dR + \int_{R_e}^{\hat{R}} q(R) N(R) dR\right], \quad \text{(S9)}$$

$$q(R) = \frac{\pi R^2 \left(\Delta T - \frac{2 T_{sat} \sigma}{R h_{fg} \rho_w}\right)}{\frac{1}{2h_{int}(1-\cos\theta)} + \frac{R\theta}{4k_w \sin\theta} + \frac{1}{k_{HC}\sin^2\theta}\left[\frac{k_P \varphi}{\delta_{HC} k_P + h k_{HC}} + \frac{k_w(1-\varphi)}{\delta_{HC} k_w + h k_{HC}}\right]^{-1}}, \quad \text{(S10)}$$

where $q$" steady state dropwise condensation heat transfer rate per unit area of the condensing surface, $\Delta T$ is the temperature difference between the saturated vapor and sample outer surface ($\Delta T = (T_{sat}(P) - T_s)$), $R^*$ is the critical radius for heterogeneous nucleation ($R^* = r_c$),[16] $R_e$ is the droplet coalescence radius, $q(R)$ is the individual droplet heat transfer (Eq. S10), $n(R)$ is the non-interacting droplet size distribution,[15] $N(R)$ is the coalescence dominated droplet size distribution,[15, 17] $R$ is the droplet radius, $\sigma$ is the condensate surface tension, $h_{fg}$ is the latent heat of phase change, $\rho_w$ is the condensate density (liquid water), $\theta$ is the droplet contact angle, $h_{int}$ is the interfacial heat transfer coefficient,[18] $k_w$ is the condensate thermal conductivity, $k_{HC}$ is the hydrophobic coating thermal conductivity, $\varphi$ is the structured surface solid fraction (≈0.023), $h$ is the structured surface height (≈1 μm), and $\delta_{HC}$ is the hydrophobic coating thickness (≈10 nm).

The first integral in equation S9 represents the heat flux component from droplets smaller than the coalescence length scale ($R < R_e$), where direct growth by vapor accommodation at the liquid-vapor interface dominates, and neighboring droplet coalescence is absent. The second integral represents the component of the heat flux from droplets growing mainly by coalescence with other droplets ($R > R_e$). These two components contribute to the total surface heat transfer per unit area ($q$").

For the jumping and flooded surfaces, the model results were obtained using experimentally determined droplet departure radii $\hat{R}$ ($\hat{R}_{dropwise}$ = 1.5 mm, $\hat{R}_{jumping}$ = 10 μm, $\hat{R}_{flooded}$ = 3 mm) and contact angles, and assuming an effective nucleation density $N$ from previous ESEM studies of condensation on CuO surfaces ($N_{nanostructured} = 3N_{smooth}$).[19] To model the individual droplet growth more accurately (for the jumping surface), the variable contact angle during the initial stages of growth was incorporated.[15]

Filmwise Condensation

To model filmwise condensation on the smooth Cu tubes, the classical Nusselt model was used, given by[8, 18]:

$$h_c = 0.729\left[\frac{g\rho_w(\rho_w-\rho_v){k_w}^3 {h_{fg}}'}{\mu_w d_{OD}\Delta T}\right]^{\frac{1}{4}}, \quad \text{(S11)}$$

$${h_{fg}}' = h_{fg} + 0.68c_{p,l}\Delta T\,, \quad \text{(S12)}$$

where $g$ is the gravitational acceleration (= 9.81m/s$^2$), $\rho_v$ is the water vapor density, $\mu_w$ is the condensate dynamic viscosity, $h_{fg}$' is the modified latent heat of vaporization accounting for the change in specific heat of the condensate and $c_{p,l}$ is the condensate specific heat .[8, 18]

**References:**


1. Balekjian, G.; Katz, D. *A.I.Ch.E. Journal* **1958,** 4, (1), 43-48.
2. Ma, X. H.; Zhou, X. D.; Lan, Z.; Li, Y. M.; Zhang, Y. *Int J Heat Mass Tran* **2008,** 51, (7-8), 1728-1737.
3. Rose, J. W. *P I Mech Eng a-J Pow* **2002,** 216, (A2), 115-128.
4. Jonsson, U.; Olofsson, G.; Malmqvist, M.; Ronnberg, I. *Thin Solid Films* **1985,** 124, (2), 117-123.
5. Nam, Y.; Ju, Y. S. *Imece 2008: Heat Transfer, Fluid Flows, and Thermal Systems, Vol 10, Pts a-C* **2009**, 1833-1838.
6. Nam, Y.; Sharratt, S.; Byon, C.; Kim, S. J.; Ju, Y. S. *Journal of Microelectromechanical Systems* **2010,** 19, (3), 581 - 588
7. Nam, Y.; Sungtaek, Y. *Journal of Adhesion Science and Technology* **2012**, 1-14.
8. Incropera, F. P., *Introduction to heat transfer*. 5th ed.; Wiley: Hobokenm NJ, 2007; p xxv, 901 p.
9. Young, E. H.; Briggs, D. E. *A.I.Ch.E. Journal* **1966,** 12, (1), 31-35.
10. Swensen, K. A. Studies on Filmwise Condensation of Steam on Horizontal Finned Tubes. Naval Postgraduate School, Monterey, 1992.
11. Miljkovic, N.; Enright, R.; Wang, E. N. *Acs Nano* **2012,** 6, (2), 1776–1785.
12. Kwak, K.; Kim, C. *Korea-Aust Rheol J* **2005,** 17, (2), 35-40.
13. Kim, S.; Kim, K. J. *J Heat Transf* **2011,** 133, (8), 081502-1 - 081502-7.
14. Vemuri, S.; Kim, K. J.; Wood, B. D.; Govindaraju, S.; Bell, T. W. *Appl Therm Eng* **2006,** 26, (4), 421-429.
15. Miljkovic, N.; Enright, R.; Wang, E. N. *J Heat Transf* **2012**.
16. Kaschiev, D., *Nucleation: Basic Theory With Applications*. Butterworth Heinemann: Oxford, 2000.
17. Rose, J. W.; Glicksman, L. R. *Int J Heat Mass Tran* **1973,** 16, 411-425.
18. Carey, V. P., *Liquid-Vapor Phase-Change Phenomena: An Introduction to the Thermophysics of Vaporization and Condensation Processes in Heat Transfer Equipment*. 2nd ed.; Taylor and Francis: New York, 2008; p xxii, 742 p.
19. Enright, R.; Dou, N.; Miljkovic, N.; Nam, Y.; Wang, E. N. *3rd Micro/Nanoscale Heat & Mass Transfer International Conference* **2012**.